SANDIA REPORT

SAND2006-6786
Unlimited Release
Printed November 2006

Modeling Injection Molding of Net-Shape Active Ceramic Components

Rekha Rao, Lisa Mondy, David Noble, Matthew Hopkins, Patrick Notz, Thomas Baer, Laura Halbleib, Pin Yang, George Burns, Anne Grillet, Carlton Brooks, Ray O. Cote, and Jaime N. Castañeda

Prepared by
Sandia National Laboratories
Albuquerque, New Mexico 87185 and Livermore, California 94550

Sandia is a multiprogram laboratory operated by Sandia Corporation,
a Lockheed Martin Company, for the United States Department of Energy's
National Nuclear Security Administration under Contract DE-AC04-94AL85000.

Issued by Sandia National Laboratories, operated for the United States Department of Energy by Sandia Corporation.

Available to DOE and DOE contractors from
U.S. Department of Energy
Office of Scientific and Technical Information
P.O. Box 62
Oak Ridge, TN 37831

Telephone: (865)576-8401
Facsimile: (865)576-5728
E-Mail: reports@adonis.osti.gov
Online ordering: http://www.osti.gov/bridge

Available to the public from
U.S. Department of Commerce
National Technical Information Service
5285 Port Royal Rd
Springfield, VA 22161

Telephone: (800)553-6847
Facsimile: (703)605-6900
E-Mail: orders@ntis.fedworld.gov
Online order: http://www.ntis.gov/help/ordermethods.asp?loc=7-4-0#online

SAND2006-6786
Unlimited Release
Printed November 2006

Modeling Injection Molding of Net-Shape Active Ceramic Components

Rekha Rao, Lisa Mondy, David Noble, Matthew Hopkins, Patrick Notz
Multiphase and Nanoscale Transport

Thomas Baer
Gram, Inc
8500 Menaul Blvd NE, Suite B-335
Albuquerque, NM 87112

Laura Halbleib
Independent Surveillance Assessment and Statistics

Pin Yang, George Burns
Ceramic and Glass

Anne Grillet
Microscale Science and Technology

Carlton Brooks, Ray O. Cote, and Jaime N. Castañeda
Thermal/Fluid Experimental Sciences

Sandia National Laboratories
P.O. Box 5800
Albuquerque, NM 87185-0836

Abstract

To reduce costs and hazardous wastes associated with the production of lead-based active ceramic components, an injection molding process is being investigated to replace the current machining process. Here, lead zirconate titanate (PZT) ceramic particles are suspended in a thermoplastic resin and are injected into a mold and allowed to cool. The part is then bisque fired and sintered to complete the densification process. To help design this new process we use a finite element model to describe the injection molding of the ceramic paste. Flow solutions are obtained using a coupled, finite-element based, Newton-Raphson numerical method based on the GOMA/ARIA suite of Sandia flow solvers. The evolution of the free surface is solved with an advanced level set algorithm. This approach incorporates novel methods for representing surface tension and wetting forces that affect the evolution of the free surface.

Thermal, rheological, and wetting properties of the PZT paste are measured for use as input to the model. The viscosity of the PZT is highly dependent both on temperature and shear rate. One challenge in modeling the injection process is coming up with appropriate constitutive equations that capture relevant phenomenology without being too computationally complex. For this reason we model the material as a Carreau fluid and a WLF temperature dependence. Two-dimensional (2D) modeling is performed to explore the effects of the shear in isothermal conditions. Results indicate that very low viscosity regions exist near walls and that these results look similar in terms of meniscus shape and fill times to a simple Newtonian constitutive equation at the shear-thinned viscosity for the paste. These results allow us to pick a representative viscosity to use in fully three-dimensional (3D) simulation, which because of numerical complexities are restricted to using a Newtonian constitutive equation. Further 2D modeling at nonisothermal conditions shows that the choice of representative Newtonian viscosity is dependent on the amount of heating of the initially room temperature mold.

An early 3D transient model shows that the initial design of the distributor is sub-optimal. However, these simulations take several months to run on 4 processors of an HP workstation using a preconditioner/solver combination of ILUT/GMRES with fill factors of 3 and PSPG stabilization. Therefore, several modifications to the distributor geometry and orientations of the vents and molds have been investigated using much faster 3D steady-state simulations. The pressure distribution for these steady-state calculations is examined for three different distributor designs to see if this can indicate which geometry has the superior design. The second modification, with a longer distributor, is shown to have flatter, more monotonic isobars perpendicular to the flow direction indicating a better filling process.

The effects of the distributor modifications, as well as effects of the mold orientation, have also been examined with laboratory experiments in which the flow of a viscous Newtonian oil entering transparent molds is recorded visually. Here, the flow front is flatter and voids are reduced for the second geometry compared to the original geometry. A horizontal orientation, as opposed to the planned vertical orientation, results in fewer voids.

Recently, the Navier-Stokes equations have been stabilized with the Dohrman-Bochev PSPP stabilization method, allowing us to calculate transient 3D simulations with computational times on the order of days instead of months. Validation simulations are performed and compared to the experiments. Many of the trends of the experiments are captured by the level set modeling, though quantitative agreement is lacking mainly due to the high value of the gas phase viscosity necessary for numerical stability, though physically unrealistic. More correct trends are predicted for the vertical model than the horizontal model, which is serendipitous as the actual mold is held in a vertical geometry. The full, transient mold filling calculations indicate that the flow front is flatter and voids may be reduced for the second geometry compared to the original geometry.

The validated model is used to predict mold filling for the actual process with the material properties for the PZT paste, the original distributor geometry, and the mold in a vertical orientation. This calculation shows that voids may be trapped at the four corners of the mold opposite the distributor.

Acknowledgments

The authors would like to acknowledge Tom Grasser for help in creating the experimental molds. We would also like to thank our reviewers Ken Chen and Harry Moffat for their timely and helpful comments. Chris Diantonio was invaluable for helping us understand the details of the injection molding process, such as mold temperature and orientation.

0

Contents

Figures

Tables

This Page Left Intentionally Blank

1. Introduction

Solid solutions of lead-based perovskites are the backbone materials of the piezoelectric components for transducer, actuator, and resonator applications. These components, typically small in size, are fabricated by grinding and lapping from large sintered ceramic slugs. These operations increase manufacturing costs and produce a large hazardous waste stream, especially when the component size decreases. To reduce the cost and hazardous wastes associated with the production of these components, injection molding techniques are being investigated to replace the machining processes. Specifically, we are studying the injection molding of a paste of lead zirconate titanate (PZT) particles suspended in paraffin wax as the basis of a net shape ceramic processing operation. The suspension is highly loaded with the ceramic particles, but a stearic acid surfactant and a polyethylene/polypropylene copolymer plasticizer are used to improve the processability of the material. The paste is injected into the mold creating the green ceramic part with the correct net shape. A schematic of the injection molder is given in Figure 1. The injection molding process starts with mixing of the solid powder components into a funnel mixer. The components are heated and pressurized to become a fluid or soft matter, depending on the temperature, at which point they are injected into the mold. Once the part is filled and cooled, the gate is broken and the part is ejected. The injection process generally takes less than ½ s and turn-around-times between parts are on the order of 5s. The part itself is small, with its longest edge length being three cm or so.

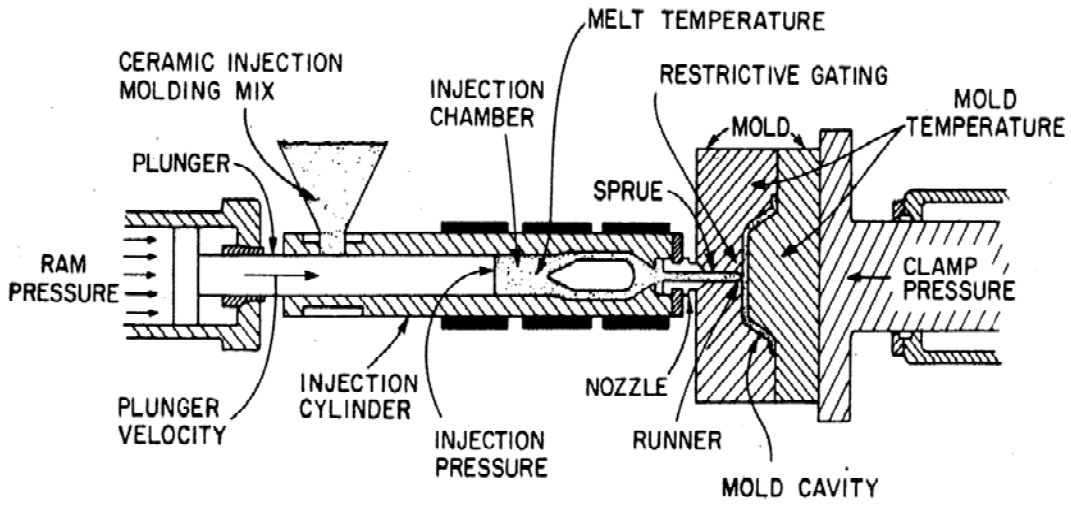

Figure 1. Schematic of injection molding apparatus.

In subsequent processing steps, the wax is burned out of the green part. The part is then sintered to create the final ceramic component. This net shape forming process is agile and inexpensive, since the final part requires no expensive grinding or retooling, thus reducing the waste stream produced.

A finite element model of the injection molding system was developed to provide insights into the filling process, to allow optimization of the die design and processing variables, and to troubleshoot potential problems such as warping, voids, and inhomogeneities. Such issues can be seen in Figure 2, which shows short shots for poorly optimized process parameters. Shorts shot are created by partially filling the mold and allowing the material to solidify, giving us a window into the injection process. Short shots can be used to understand processing parameters and potential filling problems.

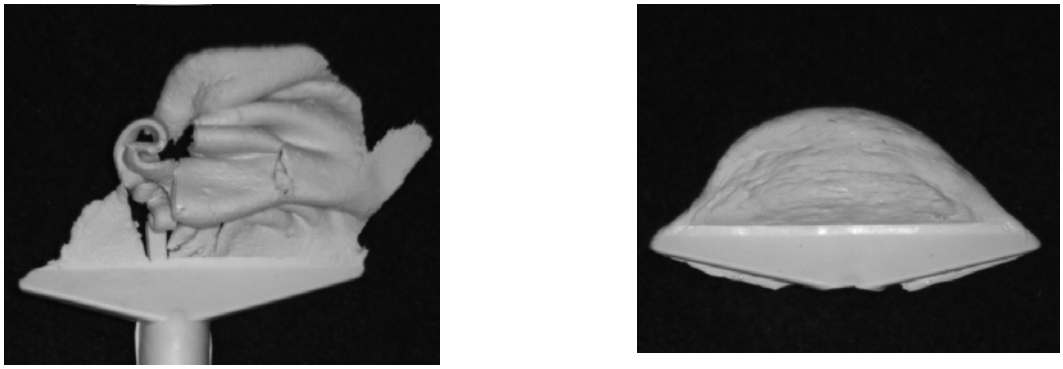

2.5 mm shot, 40% injection speed

2.5 mm shot, 100% injection speed

Figure 2. Short shots for poorly optimized process parameters.

From Figure 2, we can see that for low injection speed, e.g. low shear rates, the material behaves more like a Bingham plastic than a fluid, creating severe knit line and voids in the part. For the higher injection speed, the material behaves more like a fluid and fills the mold in a more orderly fashion.

We obtained flow solutions using a coupled, finite-element based, Newton-Raphson numerical method. The evolution of the free surface was solved with an advanced level set algorithm. This approach incorporates novel methods for representing surface tension and wetting forces that affect the evolution of the free surface [Baer et al., 2003]. In addition to modeling aspects of the proposed injection molding process, we also performed validation calculations. Specifically, we modeled a simple Newtonian fluid being injected at relatively low pressures and compared the results to experiments performed with clear plastic molds that allowed video taping of the shape and movement of the entering front.

In the next section we describe the material properties, both thermal and rheological, of the ceramic paste. Next, we describe the computational model and the numerical method, and then show preliminary results that led us to improvements in the mold design. The following section discusses the validation experiments for the original mold and the two new designs suggested by the computational work. Subsequently, we compare the validation simulations to the validation experiments and follow this with a section on simulations of the real system. We conclude with a summary of the results and ideas for future work.

2. Material Properties of PZT Ceramic Paste

2.1 PZT Ceramic Paste Thermal Properties

The thermal conductivity of the PZT paste was measured by DataPointLabs (Ithaca, NY) using a transient line source technique (ASTM D 5930 – 01). Results are shown in Figure 3.

Thermal Conductivity Data

Temp	k
°C	W/m•K
137	0.595
123	0.623
108	0.608
88	0.592
67	0.534
46	0.601
39	0.681

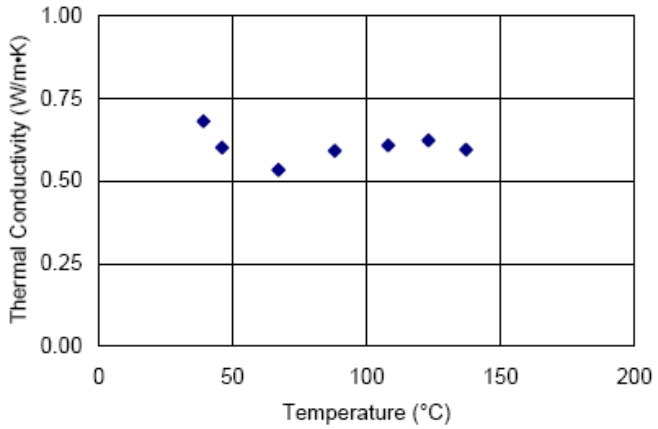

Figure 3. Thermal conductivity of PZT paste at various temperatures

The heat capacity and thermal diffusivity were also measured using differential thermal analysis and the laser flash technique, respectively. Thermal conductivity was then calculated from thermal diffusivity, density and heat capacity values. The thermal conductivity measurements were in good agreement with the transient line source technique. The average heat capacity between 130 and 150°C was 0.62 J/gK.

2.2 Rheology of the PZT Ceramic Paste

In order to perform computational simulations, we must first understand the rheology of PZT ceramic paste, i.e. how the viscosity changes with temperature and shear rate. One challenge in modeling this process is coming up with appropriate constitutive equations that capture relevant phenomenology without being too computationally complex. The paste is comprised of a highly loaded suspension of ceramic particles, in a polyethylene-polypropylene copolymer. A stearic acid surfactant is added to improve the processability of the composite material. The composition of the paste is given in Table 1 along with the density and maximum melting point for each component. The resulting density of the composite is 4.5 g/cm^3 due to the high density and high particle loading of the PZT. After being completely melted and mixed at a temperature above 150°C, the organic carrier system started to solidified at 94°C, but shows a phase transition at around 117°C.

Table 1. Composition of PZT Ceramic Paste

Material	Density (g/cm^3)	Volume %	Max. Melting point (°C)
paraffin wax	0.90-0.93	25.0	68
proflow 3000	0.92	20.3	150
Stearic acid	0.84	2.2	48
PZT particle	7.97	52.5	N/A

The viscosity of the paste was measured in a capillary viscometer, a schematic of which is shown in Figure 4. A temperature controller was used to ensure that isothermal conditions are maintained during an experiment. From the capillary viscometry, it was found that above the melting temperature of the composite of about 160°C (this value depends on the amount of solid loading and the melting temperature of the polymer matrix), the material no longer forms a coherent extrudate but starts to drip and potentially phase separate making measurements difficult. Below the melting temperature, the material must be repeatedly sheared in order to get fluid-like behavior as the paste's behavior is more like soft matter than that of a fluid.

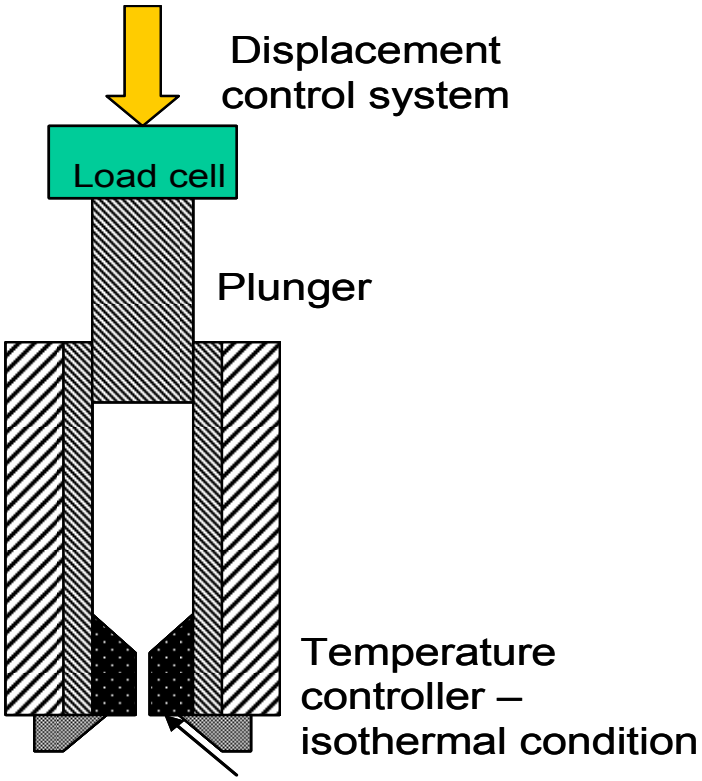

Figure 4. Capillary viscometer for viscosity measurements.

The raw stress measurements for temperature from 100°C to 135°C are shown in Figure 5 for a range of shear-rates from 0 to 1000 1/s. A phase change occurs in the paste at 117°C showing a change in shape of the stress-shear rate curve.

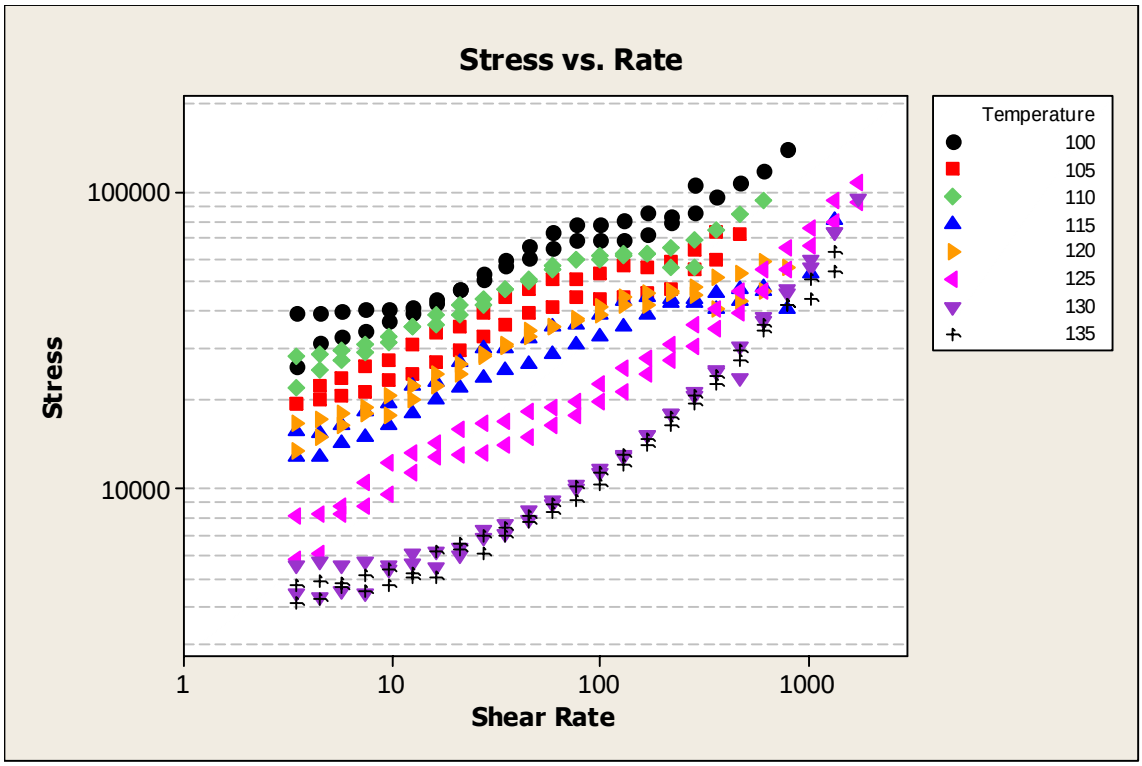

Figure 5. Raw data from capillary rheometer

The rheology of the injection-molded material exhibits shear thinning behavior, therefore, the shear rate and viscosity values must be adjusted with the Rabinowitsch correction [Ferguson & Kemblowski, 1991], since otherwise we would see 10%-20% errors in the value of the viscosity. This is because the capillary viscometer measures an apparent viscosity that would only be accurate for Newtonian fluids, not for shear-thinning ones. The Rabinowitsch correction was applied, the details of which can be found in Halbleib et al [2004]. The corrected viscosities are given in Figure 6 and show shear-thinning in a power law manner without much information on the low shear rate plateau.

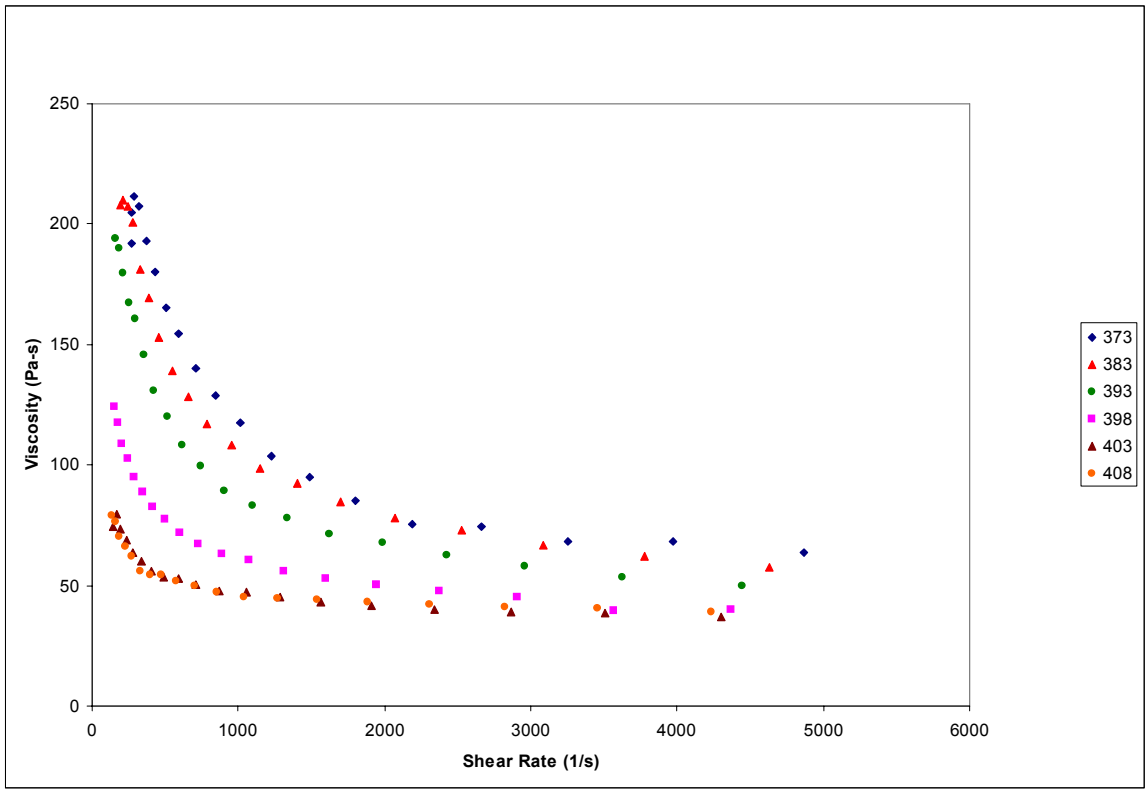

Figure 6. Viscosities after Rabinowitsch correction. Temperatures are given in Kelvin.

Because our constitutive equation will be used for computations, we need a model that will be well-behaved for the zero shear-rate limit. Power law models are not well-behaved at zero shear-rate. For this reason, we decided to use a Carreau-Yasuda model, which is well-behaved at the zero shear-rate limit, but does require values for the low and high shear-rate viscosities. These values are extrapolations, especially the low shear rate viscosity, but assuming a good fit to the experimental data of the Carreau-Yasuda parameters, it should be a reasonable representation. Here we use a Carreau-Yasuda model with a simple Arhennius temperature shift factor.

$$\mu = a_T \left[\mu_\infty + (\mu_0 - \mu_\infty)(1 + (a_T \lambda \dot{\gamma})^a)^{\frac{(n-1)}{a}} \right] \tag{1}$$

$$a_T = e^{D/T} \tag{2}$$

A non-linear least-squares Gauss-Newton method was used to estimate of D, l, a, and n, while holding μ_0 *and* μ_∞ constant. (This requires an initial guess of parameters to be estimated). Table 2 show results of the fits for a temperature of 403K or 135°C. A mean of residuals closest to 0 indicates the better fit; therefore, we used the parameters listed on the first line in Table 2 for the Carreau-Yasuda model in the isothermal 2D computations described in the following section.

Table 2. Non-linear least-squares fit of Carreau-Yasuda parameters to viscometry data at 403K

μ_0	μ_∞	n	a	λ	D	Mean of Residuals	Median of Residuals	Std Dev of Residuals
2,000	30	0.2	6.28	0.8	100	-4.93	0.206	14.65
2,000	32	0.2	6.2	0.8	100	-7.4	-2.33	14.61
2,000	35	0.2	6.06	0.8	100	-11.1	-6.13	14.55

Figure 7 shows the fit of the parameters in Table 2 as the high shear-rate viscosity is change for 403K and 408K.

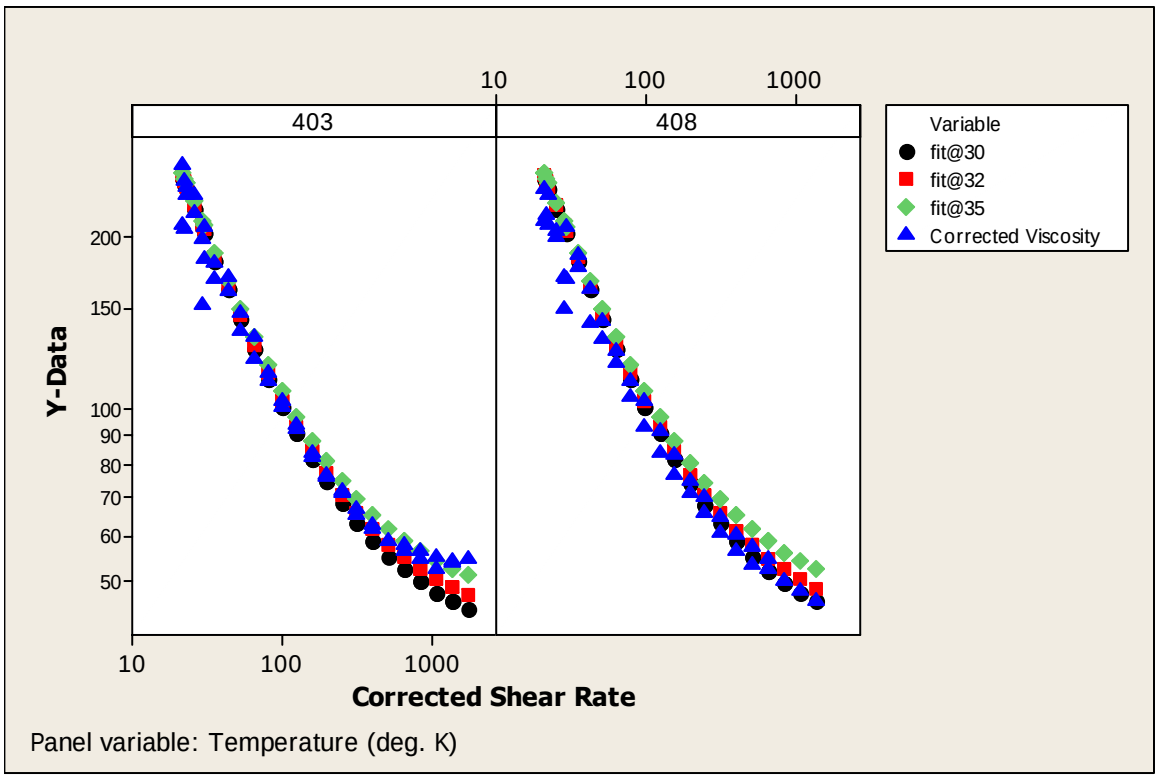

Figure 7. Plot of fitted viscosity (Pa s) versus the corrected experimental viscosities as a function of shear rate, at 403K and 408K. The high shear rate viscosities for the fit are varied from 30 Pa s, to 32 Pa s, and 35 Pa s.

From Figure 7, we can see that fit giving the smallest residual has a high shear-rate viscosity of 30 Pa s, and this set of parameters from row 1 of Table 2 fits the data well at 408. Unfortunately, the high shear rate viscosity of 35 Pa s fits the data better at 403. It is very difficult to fit the data for a range of temperatures and shear rates, and the most we can hope is to capture the trends from the data with the Carreau model.

We also tried to fit the rheology to a Carreau model that used the Williams-Landel-Ferry (WLF) [Williams et al. 1955] type of shift factors hoping to be able to capture the change of shape in the viscosity curves as they undergo a phase transition.

$$\mu = a_T \left[\mu_\infty + (\mu_0 - \mu_\infty)(1 + (a_T \lambda \dot{\gamma})^a)^{\frac{(n-1)}{a}} \right] \tag{3}$$

$$a_T = \exp[\frac{c_1(T_{ref} - T)}{c_2 + T - T_{ref}}] \tag{4}$$

Figure 8 shows a fit to the Carreau-WLF model, which was done with an excel spread-sheet and a visual representation of the fit to the data. The fit emphasizes the high temperature data, where it represents the experimental data reasonably well, but does a poorer job for lower temperatures. We felt that for the material being injected at a temperature of 405K, a good fit to the hot temperature rheology would be more important than a good fit to the lower temperature rheology. This may or may not be true depending on the boundary conditions used for the simulation, as discussed in the nonisothermal modeling section.

The values for the Carreau-WLF parameters are given in Table 3.

Table 3. Carreau-WLF parameter for Non-isothermal Modeling

Carreau-WLF parameter	Value
low shear-rate viscosity, μ_o	50,000 Poise
high shear-rate viscosity, μ_{oo}	350 Poise
Power-law coefficient, n	0.32
Time constant, λ	2.67s
Scale factor, a	1.915
WLF parameter, c_1	50
WLF parameter, c_2	1600
WLF reference temperature, T_{ref}	390K

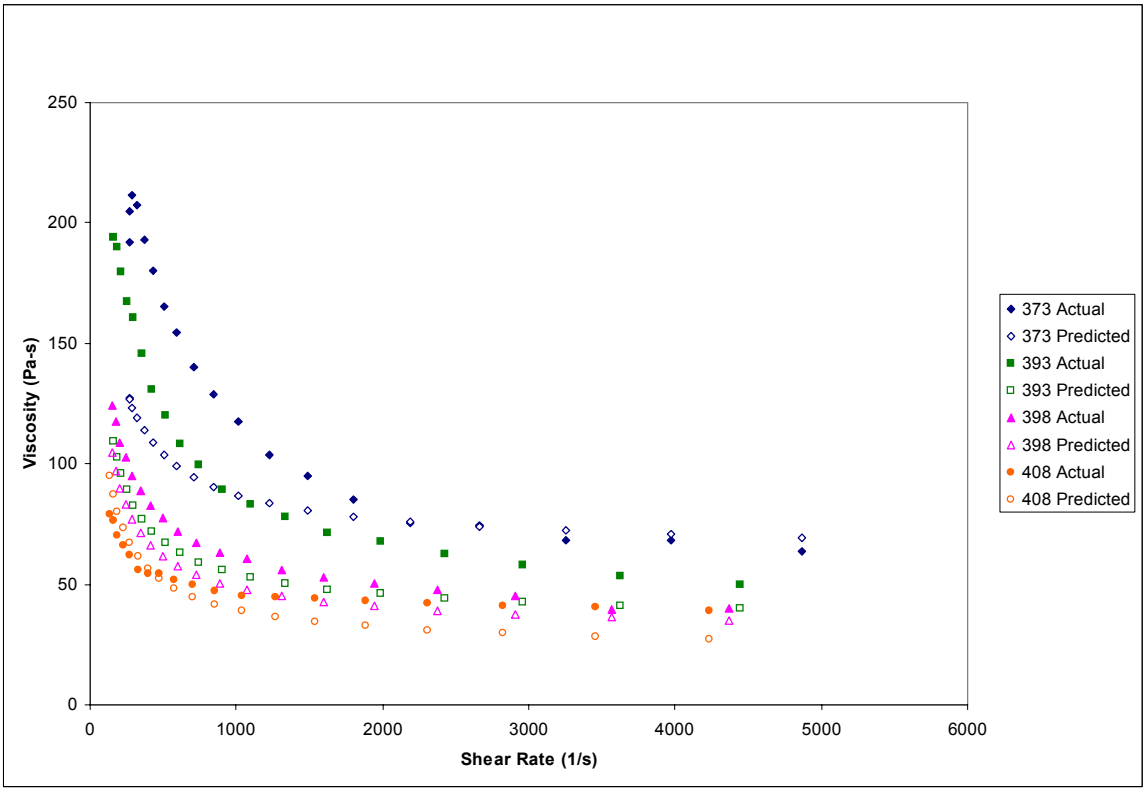

Figure 8. Viscosity predicted from Carreau-WLF fit versus thermal data for 373K, 393K, 398K, and 408K. The fit favors the higher temperatures.

3. Computational Models, Method and Preliminary Results

3.1 Fluid Mechanics Equations and Level Set Theory

In order to model mold filling of the PZT slurry as it displaces the air in the mold, we need to be able to understand both the fluid flow and its interaction with the free surface. To this end, we couple the equation of motion with a level set method to determine the location of the evolving free surface.

The equations of motion for the flow of incompressible, viscous Newtonian and non-Newtonian fluids are as follows. First, we have conservation of momentum

$$\rho \frac{Du}{Dt} = \nabla \bullet (\mu(\nabla u + \nabla u^t) - \nabla p + \rho g + f \tag{5}$$

and conservation of mass for incompressible fluids with constant density.

$$\nabla \bullet u = 0 \tag{6}$$

Here u is the fluid velocity, p is the pressure, t is time, g is the gravitational acceleration, and f includes all other body force terms. The material properties, density, ρ, and viscosity, μ, seen in Equation (5) end up as functions of both the material and the level set equation.

The level set method of Sethian [1999], a front capturing scheme, is used to determine the evolution of the interface with time. The level set is a scalar distance function, the zero of which coincides with the free surface or fluid-gas interface, *e.g.*

$$\phi(x, y, z) = 0\,. \tag{7}$$

We initialize this function to have a zero value at the fluid-gas interface, with negative distances residing in the fluid phase and positive distances in the gas phase. An advection equation is then used to determine the location of the interface over time.

$$\frac{D\phi}{Dt} = 0 \tag{8}$$

Derivatives of the level set function can give us surface normals, n, and curvature, H, at the interface useful for applying boundary conditions.

$$\begin{aligned} n &= \nabla \phi \\ H &= \nabla \bullet \nabla \phi \end{aligned} \tag{9}$$

Material properties vary across the phase interface from the properties of the fluid to the properties of the displaced gas. This variation is handled using a smooth Heaviside function that modulates material properties to account for the change in phase.

$$\rho(\phi) = \rho_{fluid} + (\rho_{gas} - \rho_{fluid}) H_\alpha(\phi), \qquad -\alpha < \phi < \alpha \tag{10}$$

$$\mu(\phi) = \mu_{fluid} + (\mu_{gas} - \mu_{fluid}) H_\alpha(\phi), \qquad -\alpha < \phi < \alpha \tag{11}$$

$$H_\alpha(\phi) = \frac{1}{2}(1 + \frac{\phi}{\alpha} + \frac{1}{\pi}\sin(\frac{\pi\phi}{\alpha})) \quad (12)$$

This is a diffuse interface implementation of the level set method, which allows for a mushy interfacial zone of length 2α, in which the properties will vary from fluid to gas values. Note that this method can be applied to both Newtonian and non-Newtonian fluids.

Surface tension is applied using a continuous surface stress formulation using a smooth Dirac delta function that applies this force only at the interface [Jacqmin, 1995].

$$\mathrm{T} = \sigma\delta_\alpha(\phi)(\underline{I} - nn) \quad (13)$$

$$\delta_\alpha(\phi) = \left(1 + \cos\left(\frac{\pi\phi}{\alpha}\right)\right)/2\alpha \quad (14)$$

When using an advection equation to evolve the level set equation over time, difficulties arise as to preserving the distance function away from the interface. This is because Equation (8) only truly holds at the interface itself and using an advection equation will not preserve the distance function away from the interface. For this reason, a Huygens' algorithm is used to periodically redistance the level set function to maintain it as a distance function [Sethian, 1999].

3.2 Numerical Method

The equations of motion (5, 6), and the advection equation for the level set, Equation (8) are solved with the finite element method. The 2D simulations were done with GOMA [Schunk et al., 2006] using a fully-coupled, Newton-Raphson numerical method and an LBB element of biquadratic velocity and level set, and bilinear pressure. The discretized equations were solved with a direct Gaussian elimination method.

The 3D simulations were done with ARIA [Notz et al., 2006] using a coupled velocity-pressure solve, and a decoupled level set equation. The Navier-Stokes equations were stabilized with the Dohrman-Bochev pressure stabilized pressure-projection (PSPP) [Dohrmann and Bochev, 2004] to allow for equal order, bilinear, interpolation of all variables. This stabilization method greatly improved the condition number of the discretized matrix equations, allowing for the use of an ILU preconditioner with a BiCGStab Krylov iterative solver. This was much more efficient than the previous stabilization method used, pressure stabilized Petrov-Galerkin (PSPG) [Droux and Hughes, 2000], which would allow equal order interpolation, but required a costly ILUT preconditioner with up to three levels of fill and a more expensive GMRES iterative solver. Because of the improvements of stabilization, using PSPP/ILU/BiCGStab, we ended up with computation times on the order of days instead of months for the previous method, PSPG/ILUT(3)/GMRES. Scalability was also greatly improved, allowing simulations to be run in parallel on 64 processors, giving turn around times of hours. This enabled transient design calculations on several meshes to be completed in a day.

Both the GOMA LBB simulations and the ARIA stabilized simulation showed good mass conservation when the constant inflow velocity results for mass as a function of time are compared to the analytical solution.

3.3 2D Mesh and Boundary Conditions

For the 2D simulations, we used an axial cross-section of the actual geometry, which could represent a 2D slice down the center of the distributor and mold. We did this because we wanted to look at nonisothermal and non-Newtonian effects, both of which require fine meshes. We felt it was best to begin with 2D simulations and debug the input decks and boundary conditions before moving on to 3D simulations.

The mesh and boundary conditions are given in Figure 9. The mesh contains 2244 9-node hexahedral elements with 9321 nodes, resulting in 30380 total degrees of freedom for the biquadratic velocity/bilinear pressure LBB element used in combination with biquadratic level set interpolation. For nonisothermal simulations, a temperature field was added using a bilinear interpolation. In addition, the streamline-upwinding Petrov-Galerkin method (SUPG) was used to stabilize the temperature field.

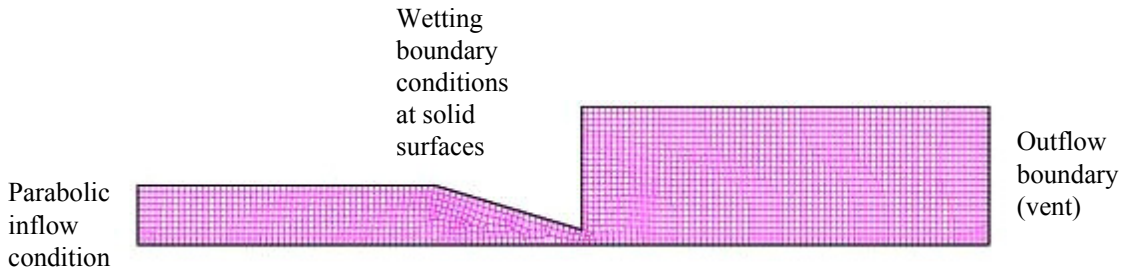

Figure 9. FEM mesh and boundary conditions for 2D mold filling.

The boundary condition on the inflow boundary is a constant parabolic inflow velocity for both the isothermal Newtonian and Carreau fluid.

$$v = v_{\max}(1 - y^2) \tag{15}$$

This is the exact solution for Poiseuille flow of a Newtonian fluid between two plates and only an approximation to the correct form for a Carreau fluid [Bird et al, 1987].

The velocity is taken so that the mold fills in about 0.25s, which is comparable to the injection time in the real system, though the real system has a constant pressure inflow condition so that the velocity will vary throughout the filling process. The outflow boundary is open for the venting of the mold filling process. The solid surfaces use wetting boundary conditions as follows. We apply no penetration in the normal direction

$$n_w \cdot v = 0 \tag{16}$$

and use a Navier slip condition for the tangential velocity.

$$\tau_{slip} = \frac{1}{\beta(\phi)} v_{fluid} \tag{17}$$

Here β, the Navier slip coefficient, varies from a large value near the contact line to a small value away from the contact line to enforce no slip away from the interface.

A linearized Blake model [Blake and Haynes, 1969] enforces the dynamic contact angle condition in the interfacial region by applying a force proportional to the difference between the static and dynamic contact angles..

$$\tau_{wetting} = \frac{1}{c_T}(\cos(\theta) - \cos(\theta_S))\delta_\alpha(\phi) \qquad (18)$$
$$n \cdot n_w = \cos(\theta_s)$$

Here θ is the dynamics contact angle, θ_s is the static contact angle, and $1/c_T$ is the inverse of the wetting speed.

The density of air at the relevant temperature of 398K is 0.0011g/cm^3 and the viscosity is 2.17x10^{-4} Poise. Numerically, we use a density of the displace air phase of 0.001 g/cm^3 and a viscosity of 0.001 Poise, which is roughly ten times higher that the actual value.

3.4 Results of 2D mold filling -- Isothermal

2D isothermal mold filling was carried out for a Newtonian fluid and a Carreau fluid. The Newtonian solution uses a constant viscosity of 1000 Poise and density of 4.5 g/cm^3. The Carreau fluid uses the parameters discussed in the first part of section 2.2 and summarized in Table 2, ignoring any nonisothermal effects. The filling profiles from the finite element/level set solutions for both fluids are given in Figure 10. From this Figure, we can see that the shape of the interface is similar for both the Newtonian and shear-thinning fluid implying that the wetting physics dominate the shape of the interface. We use the same wetting parameters for both simulations. The Carreau fluid simulations show viscosities ranging from 20,000 Poise in the center of the plates and at the free surface to 300 Poise in the narrowest region of the distributor. The average wall viscosity for the Carreau fluid ends up being about 390 Poise. The entire range of viscosity is seen for the Carreau fluid in the simulations. Once we see the solidification-type behavior at the free surface, the material on the free surface no longer flows but moves via a solid-body translation. However, this complexity does not seem to have an effect on the shape of the free surface.

The shear-thinning fluid fills slightly faster than Newtonian fluid, mostly because the wall of the mold sees a value of 390 Poise for the Carreau fluid while the Newtonian mold wall sees a viscosity of 1000 Poise. The 2D simulations for both fluids imply that a bubble could be trapped in the corner above the distributor inflow into the mold.

Based on the 2D simulations, it was determined that 3D filling simulations using a Newtonian model would be enough to troubleshoot the mold design and to provide guidance on possible redesigns, as the wetting physics and wall viscosity seem to be the dominant parameters affecting the shape of the interface and filling rate.

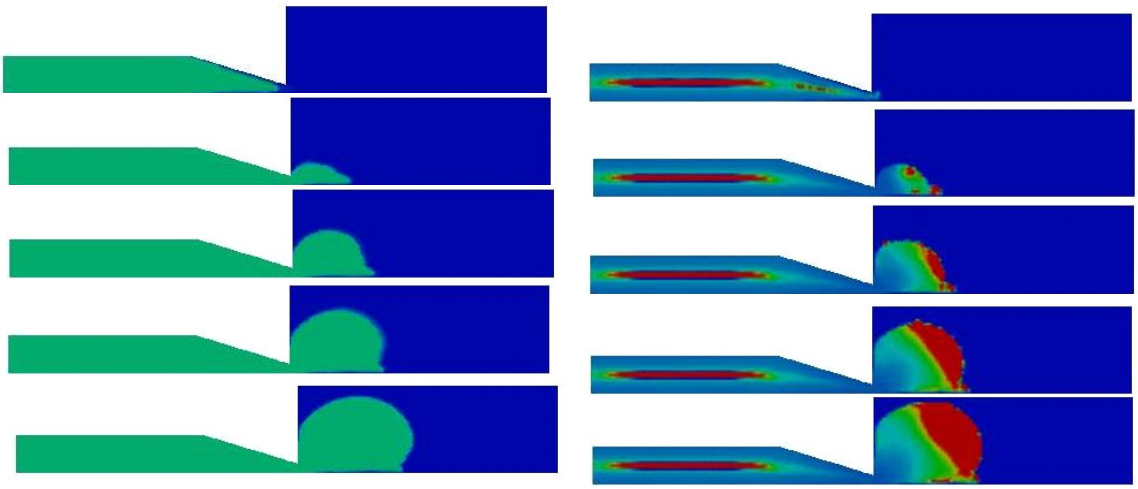

Figure 10. Comparison of Newtonian and highly shear-thinning Carreau models for 2D mold filling. The Carreau model viscosity ranges from 20,000 to 300 Poise. Red values of the viscosity are clipped above 4000 Poise.

3.5 Results of 2D mold filling -- Nonisothermal

The process is nonisothermal, and the paste has complex, temperature and shear-rate dependent rheology as seen in Section 2.2 and summarized in Table 3. The Carreau model with the temperature dependence discussed in Section 2.2 was used here to represent the behavior of the viscosity. In our simulations, we assumed that we could ignore the heat transfer effects of the steel mold and represent it via boundary conditions.

The first nonisothermal simulation we performed used an injection temperature of 383K, room temperature walls, 298K, and a pressure inflow of 4.0e6 dyne/cm^2. This assumes that the stainless steel mold stays at room temperature during the injection process by providing enough thermal mass compared to the part that temperature variations in the mold can be ignored. Since the mold is on the order of a foot and the part is on the order of an inch, this is a good assumption small distances away from the part, though the mold will likely heat up close to the part. We feel that room temperature wall will give us the highest viscosity possible, giving us an upper bound on the wall viscosity. The injection pressure is lower than the actual pressure, as it gives a fill time of seconds instead of less than 0.5s as seen for the actual process. This was due to the lack of convergence of the numerical method for faster injection speeds, probably due to too fast changes in viscosity over time that could not be captured by the numerical method. The temperature profiles for this simulation are given in Figure 11.

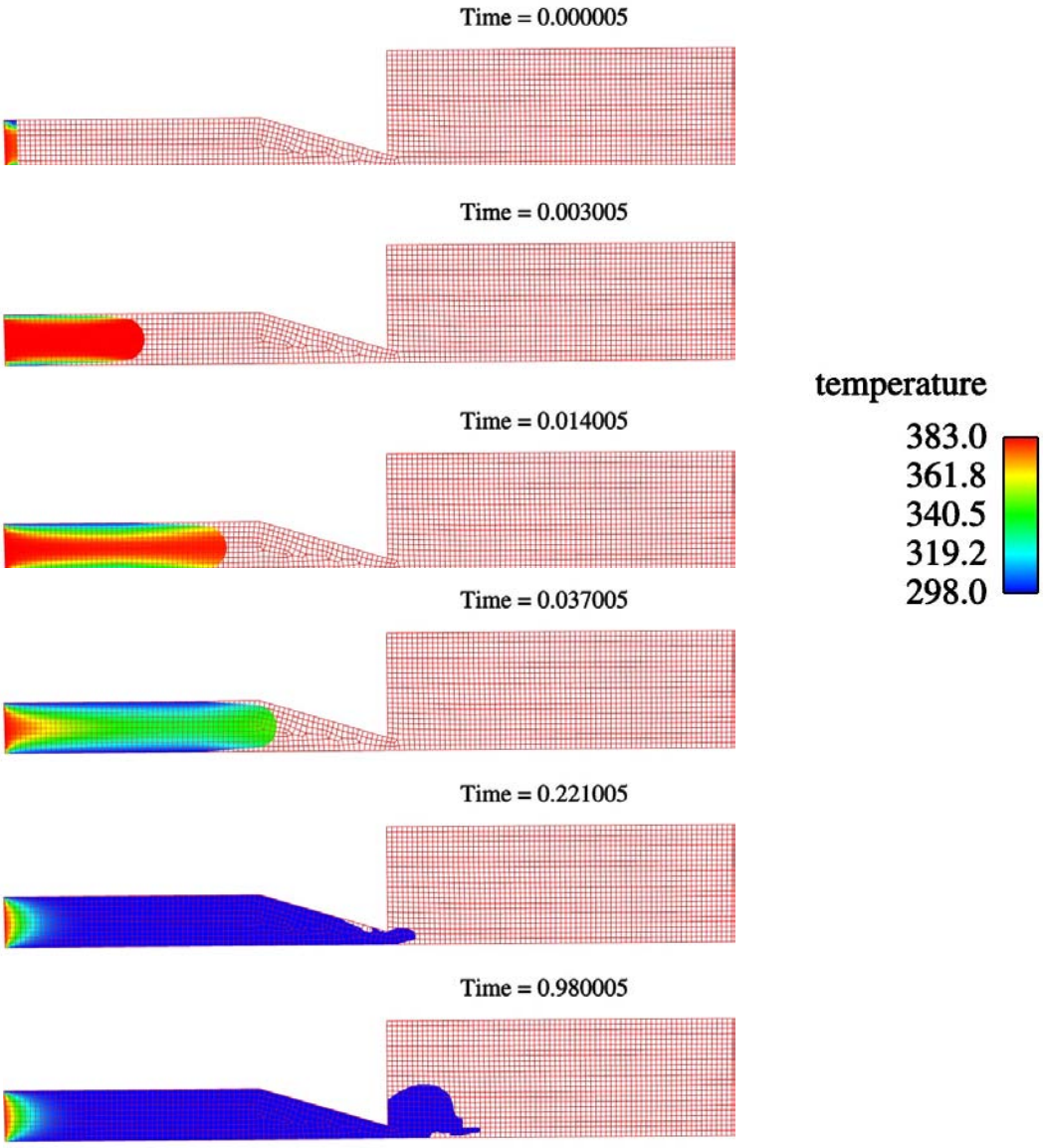

Figure 11. Temperature as a function of time for room temperature walls and pressure inflow condition.

From Figure 11, we can see that the hot liquid enters the mold and stays hot for only milliseconds. By 0.014s the wall cools the hot liquid and by 0.037s the wall region is at room temperature. By 0.22s the material is at room temperature everywhere but at the inflow. Figure 12 shows the viscosity at early and late times.

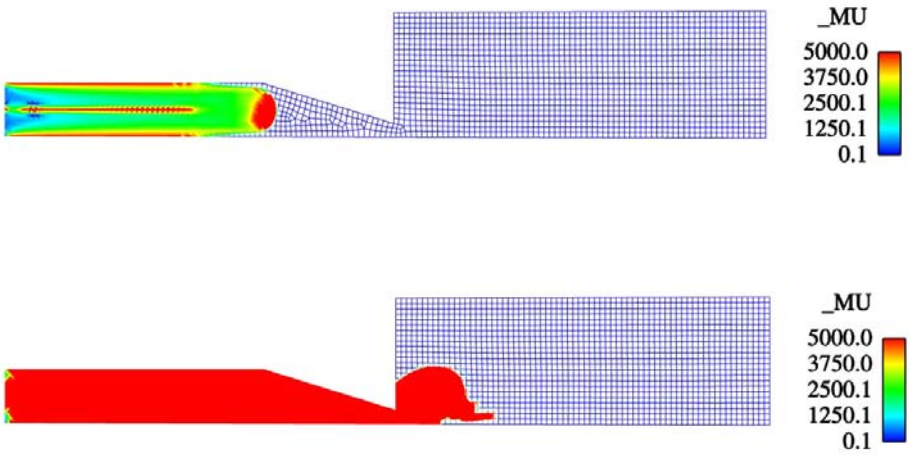

Figure 12. Viscosity for early and late times for room temperature walls. Viscosity is clipped above 5000 Poise to allow us to see the range of viscosity. Temperature and shear rate gradients occur at early time showing a range of viscosity. For late times, the fluid becomes isothermal and exhibits a constant, high viscosity of roughly 11,000 Poise.

At early times, we see gradients in the value of viscosity. The viscosity is high at the channel walls due to cooling, and high at the center of the channel and at the free surface due to low shear rate. At later times, the viscosity takes on a constant value of roughly 11,000 Poise since the material is mostly isothermal.

Because of uncertainty in the wall boundary conditions for the temperature equation, we also examined a case where a heat transfer coefficient was used to represent the fact that the steel mold is initially at room temperature, but then heats up over time. Here the boundary condition is:

$$q = h(T - T_{room}) \qquad (19).$$

The value of the heat transfer coefficient was chosen somewhat arbitrarily to be 2.5×10^7 erg/cm^2 s K. This value is probably low for steel. This simulation uses a parabolic velocity inflow condition to yield filling in less than 0.5s. Temperature profiles as a function of time are given in Figure 13 for the heat flux boundary condition based on a heat transfer coefficient.

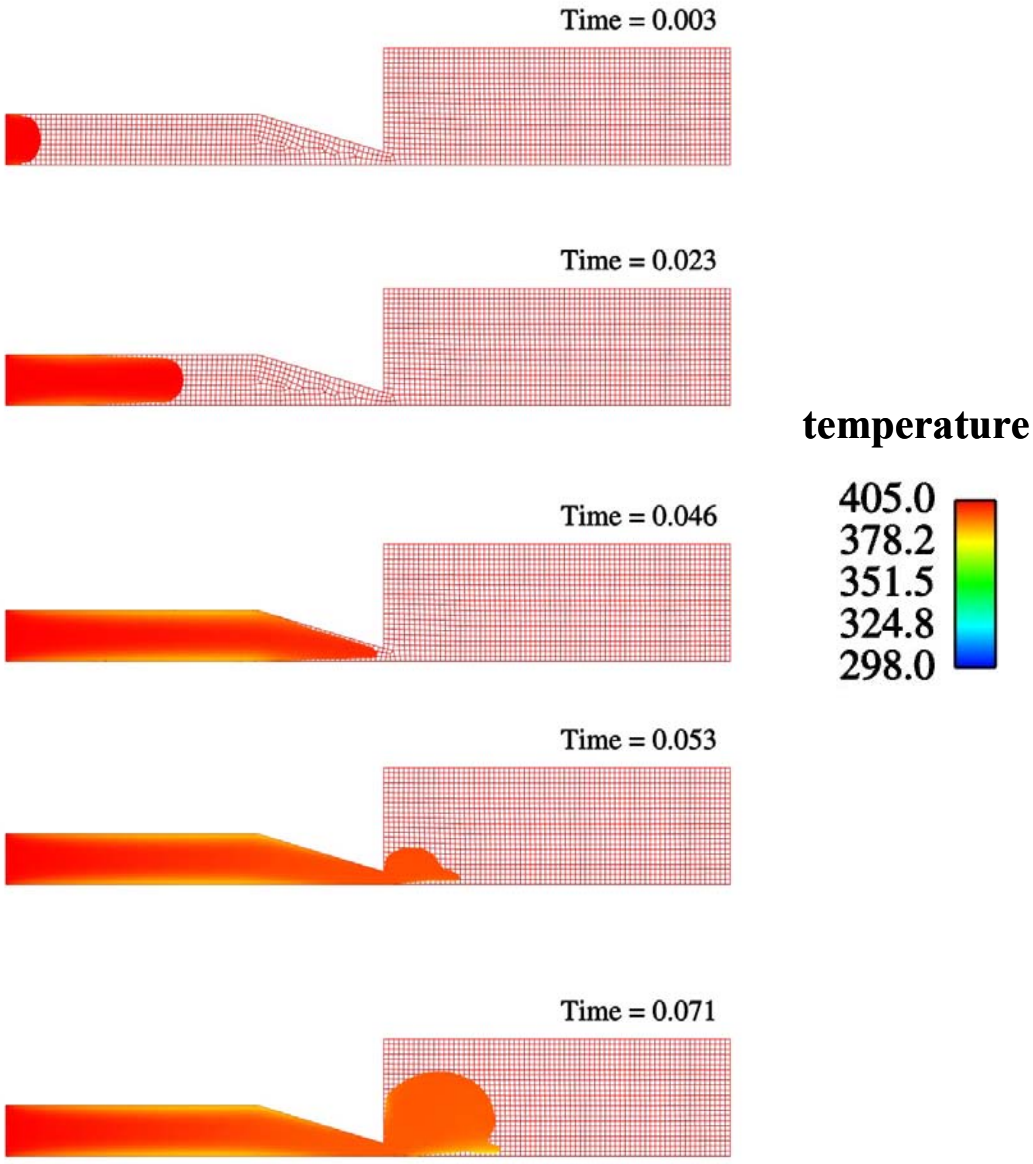

Figure 13. Temperature as a function of time for simulations with thermal boundary condition of heat flux based on a heat transfer coefficient at walls.

From Figure 13, we can see that the temperature remains almost isothermal at the high inflow value of 405K with only slight cooling near the walls down to a value between 385 and 390K. Figure 14 shows the resulting viscosity at late times, which shows changes for shear-rate at the free surface and at the center of the channel. The value of the viscosity at the small channel walls is roughly 620 Poise.

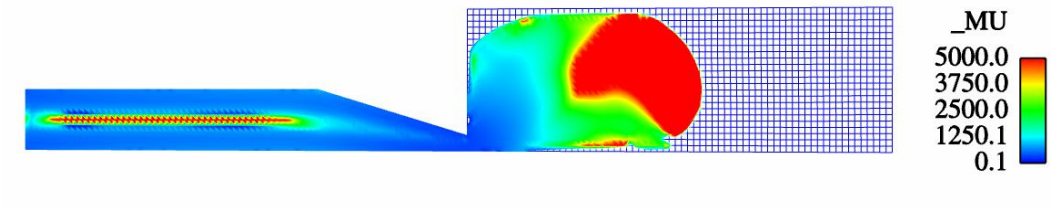

Figure 14. Viscosity at late times for heat transfer coefficient based boundary condition at wall. Viscosity is clipped above 5000 Poise to allow us to see the range of viscosity.

The disparity between the results for room temperature walls and the heat flux based on a heat transfer coefficient wall boundary conditions led us to believe that the heat transfer at the wall needs to be represented better. Because of this, a transient thermal analysis was carried out for 0.5s with the paste at an initial temperature of 405K and the stainless steel mold at room temperature. In this analysis, the walls of the mold did heat up to about 340K and came down to a steady value of 320K. This result is somewhat of a simplification, since the mold actually see many heating and cooling cycles, as the green ceramic parts are being continuously produced, with injections time of hot paste lasting less than 0.5s, to cooling and then ejection after 5s. However, this should be a reasonable temperature value for the processing step. For future work, we plan to include the steel mold in the nonisothermal simulations coupled with the level set. However, we have used these simulations to bracket the viscosity range seen for the real process between 620 Poise and 11000 Poise. For the 3D simulations of the real process we will use a viscosity of 4000 Poise, which corresponds to the viscosity at walls of temperature 320K.

3.6 Initial 3D mesh, boundary conditions, and preliminary results

The initial 3D mesh and boundary conditions are given in Figure 15 for the isothermal mold filling simulations. We assume symmetry about the centerline and only solve half the problem to improve the computational efficiency. The mesh contains 6744 8-Node hexahedral elements giving 41300 total degrees of freedom for bilinear velocity/bilinear pressure interpolation. This non-LBB element requires Petrov-Galerkin Pressure stabilization (PSPG) to allow for equal order interpolation and to reduce the condition number of the matrix due to the zero on the diagonal for the continuity equation. This method adds the residual of the momentum equation weighted with the derivative of the pressure shape function to the continuity equation, creating a nonzero diagonal. However, this stabilization method can cause problems with mass conservation if large values of the PSPG prefactor are used. Thus, only enough stabilization is used to maintain both mass conservation and convergence of the iterative solvers. Sadly, this amount of stabilization results in a matrix with a large condition number that necessitates ILUT preconditioning with fill factors of 3 and a GMRES indirect solver. This leads to long solutions times, on the order of months for parallel simulations run on 4 processors of three HP workstations.

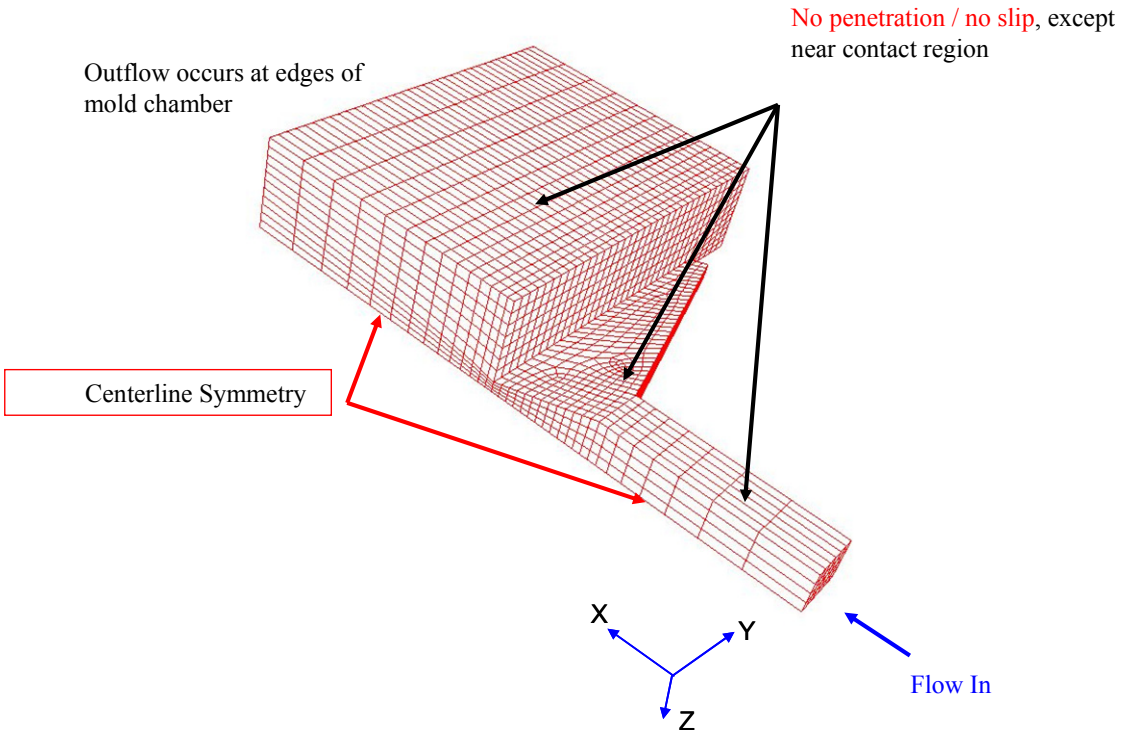

Figure 15. Initial mesh and boundary conditions for 3D level set simulations. The outflow vent is on the same side as the distributor for vertical simulations and opposite the distributor for horizontal simulations.

For the preliminary 3D simulations, we used the wetting model discussed in Section 3.2 with a liquid density ρ_{liq} of 4.5 g/cm3, a gas density ρ_{gas} of 0.0045 g/cm3, an incompressible, Newtonian liquid viscosity of μ_{liq} of 1000 P and an incompressible gas viscosity μ_{gas} of 125 P. Since it is a high capillary number flow, surface tension effects have been neglected with a numerical value of the surface tension of σ= 1.0 dyne/cm being used. Results of the meniscus shape as a function of time from these preliminary simulations are given in Figure 16. These simulations assume gravity is perpendicular to the flow direction parallel to the symmetry plane, i.e. in a horizontal orientation.

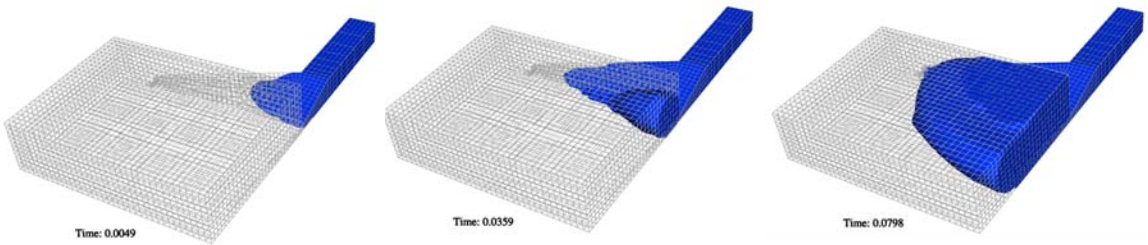

Figure 16. Preliminary simulations using PSPG in a horizontal orientation

From Figure 16, we can see that the fluid enters the main cavity before completely filling the distributor, which then lead to pooling of the fluid in center of the cavity. We also see the fluid wets the bottom surface before the top surface and shows some slumping due to gravity. These preliminary simulations led us to believe that the shape of the distributor could be improved to reduce pooling in the center of the cavity. This work will be discussed in the following section.

3.7 Distributor redesign and steady-state results

We tried some minor redesigns to the distributor to see if we could improve the flow into the mold and reduce pooling in the center of the mold. Ideally, we would like to see a flat profile coming out of the distributor and a more one-dimensional front shape. Figure 17 shows the original mesh, Mesh1, and a variation, Mesh 2, with a longer distributor, and Mesh 3 with a longer-taller distributor. The idea behind Mesh 2 was to give a longer length for the flow to develop a flat profile and fill up the distributor before entering the main cavity. Mesh 3 kept this longer distributor and made it wider on inflow to ease the fluid entering the cavity. These ideas were inspired by discussions in Sartor [1990] about die design. The meshes themselves all have the same cavity size and a similar amount of refinement, though Mesh 2 and Mesh 3 have more elements and unknowns due to the longer distributor.

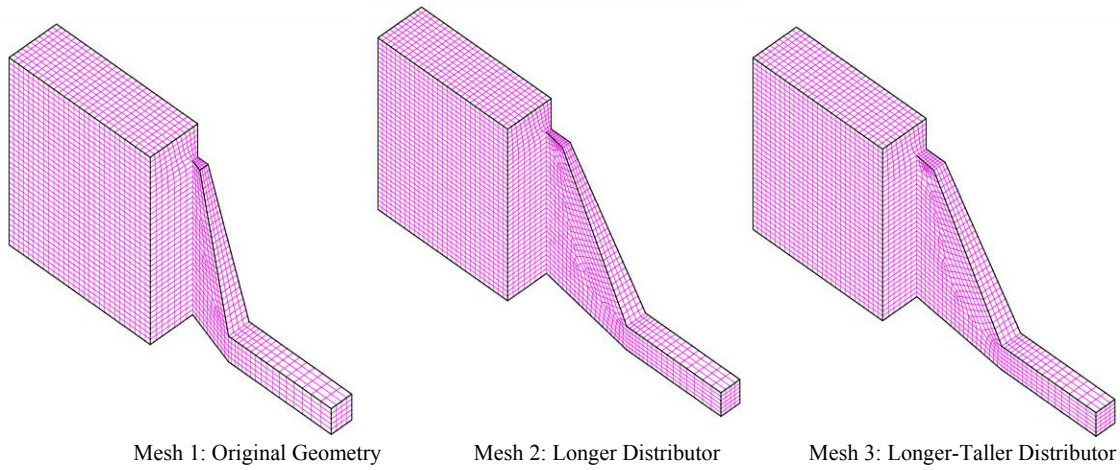

Figure 17. Redesign of the distributor: Mesh 1, Mesh 2, Mesh 3.

Since the transient simulations were taking on the order of weeks or months to run, we decided to run steady-state fluid flow without the level set to determine the pressure profile as a way to estimate the results that true transient mold filling simulations would give. Figures 18-20 show the velocity and pressure fields on a slice plane at the inflow of the cavity from the distributor for Mesh 1, Mesh 2 and Mesh 3. The x-y plots of the pressure and velocity components are taken at the center of the distributor on the slice plane. Here v_y is in the flow direction.

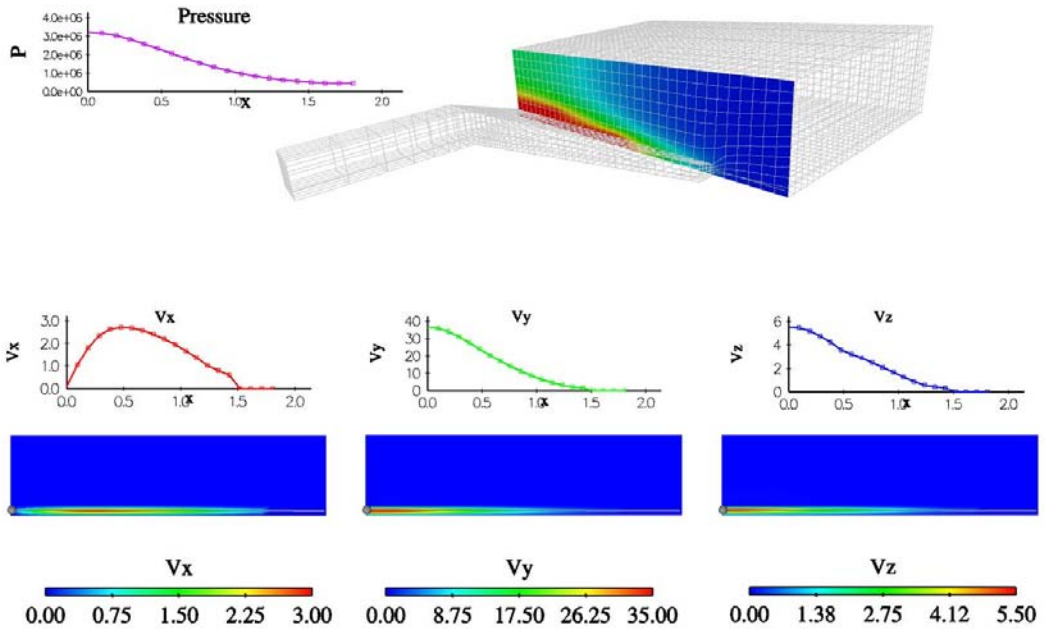

Figure 18. Steady-state velocity and pressure fields at the inflow of the cavity for Mesh 1.

Figure 18 shows that there is a gradient of pressure in the distributor as it opens to the cavity with the highest pressure seen at the center of the channel. Ideally, we would like the pressure to be flat along the wall. The axial velocity also indicates that pooling will occur in the center of the channel since it reaches its maximum at the symmetry plane.

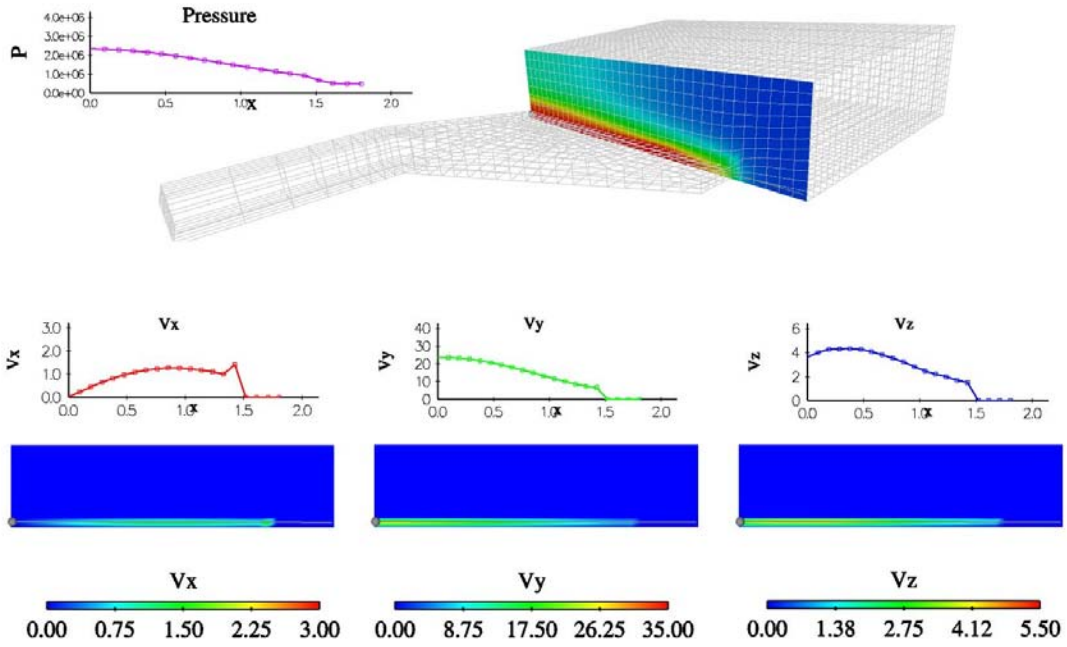

Figure 19. Steady-state velocity and pressure fields at the inflow of the cavity for Mesh 2.

The results for Mesh 2 given in Figure 19 show a pressure gradient, but less severe than Mesh 1. The pooling of the velocity in the center of the mold is also less pronounced

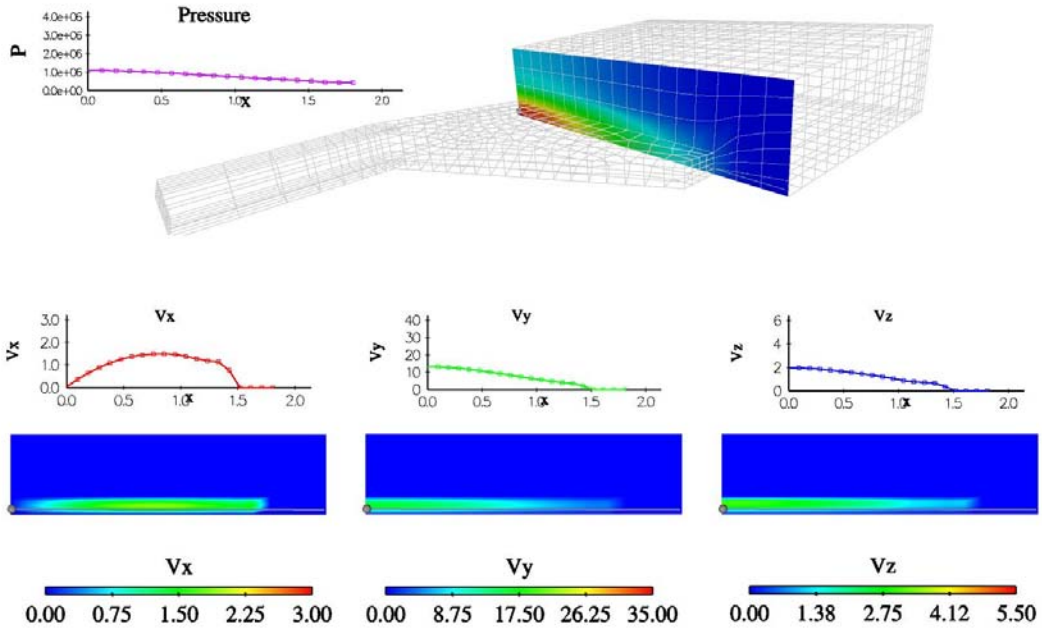

Figure 20. Steady-state velocity and pressure fields at the inflow of the cavity for Mesh 3.

The results for Mesh 3 shown in Figure 20 show a lower over all pressure, but a pressure gradient with its highest value near the symmetry plane. The lower pressure also indicates a lower velocity and shear-rate, which may make it difficult to get our real material, a shear-thinning ceramic paste into the mold. However, the results for this mesh also look better than Mesh 1, though not as good as Mesh 2. From our results, we have concluded that a longer distributor, such as that seen in Mesh 2, could improve the injection molding process by reducing void size.

4. Validation Experiments

It was decided to visually record the flow of a simple, single phase, Newtonian liquid through transparent molds to validate the front tracking and wetting models used in the computations. For these tests, we built transparent acrylic molds identical to the three mesh geometries. A fourth geometry was also tested. In this fourth case, the distributor was stretched across the entire mold in the y-direction but was held to the same x- and z-dimensions as those of Mesh 2.

The strength of the acrylic material making up the transparent molds dictated that we inject at a lower injection pressure and lower operating temperature than the actual process. To mimic the actual injection process, we used a pressure driven syringe held at a constant pressure of 29.95 ± 0.10 psig during injection. These conditions resulted in an injection rate that was approximately ten times slower than the actual process. We chose a liquid with a viscosity that was similar to the PZT paste at the walls where it had shear-thinned to a low value. The Reynolds number for the actual process and the validation experiments were similar and in the Stokes regime of much smaller than one. The syringe plunger was modified with an extra o-ring to minimize air leakage around the seal. The time to fill the molds varied from test to test, but was determined and recorded for each test.

The liquid used was a lubricant, UCON 75-H-90,000, an oxyethylene/oxypropylene. Before this liquid was injected, it was held in a water bath at a constant temperature of 23.5^{o}C. The viscosity, surface tension, and wetting properties of the UCON lubricant were determined at this temperature. The viscosity of the lubricant was measured with a Rheologica™ constant stress rheometer and was equal to 39 Pa-s over a shear rate ranging from 0.1 to 10 sec^{-1}. The surface tension measured with a Du Noüy ring (mean circumference of 5.935 cm) was 42.4±0.1 dyne/cm. The dynamic contact angle on acrylic was measured with a feed-through goniometer (Brooks, 2006), in which liquid can be continuously injected to achieve “high” velocities, or the sessile drop can be allowed to relax to obtain “low” velocities. Figure 21 is a schematic of the experimental apparatus. Figure 22 shows the results of these wetting tests.

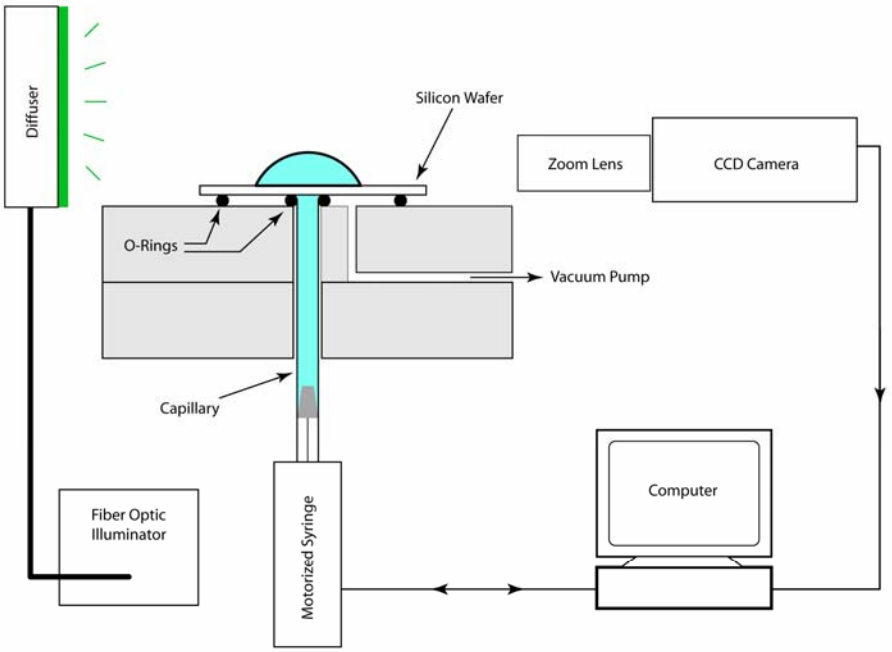

Figure 21. Sketch of apparatus for wetting parameter measurements.

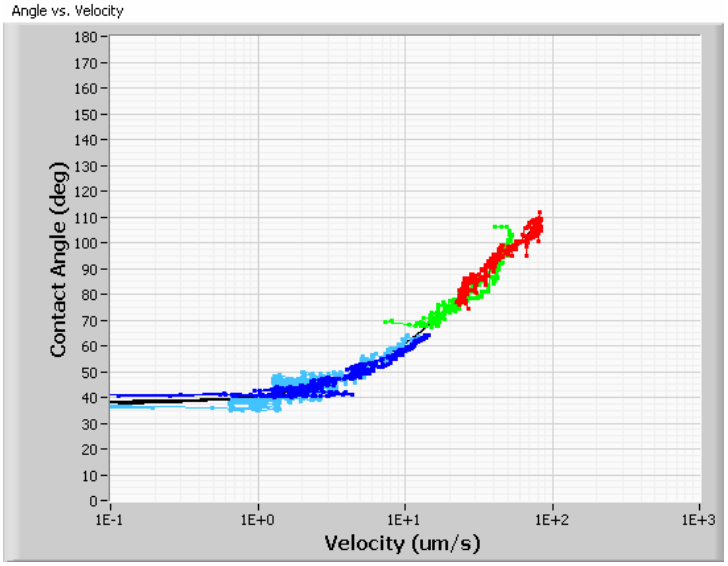

Figure 22. Dynamic wetting measurements of contact angle vs. velocity for 75-H-90000 Ucon on acrylic.

Figures 23 and 24 are representative frames from the video recordings of the fill process using a vertical alignment of the mold as in the proposed process. The time it took to completely fill the original geometry (so that liquid beginning to exit along the entire length of the vent) was 24.6 ± 1.2 s, to fill the geometry of Mesh 2 was 26.9 ± 2.0 s, and to fill the geometry of Mesh 3 was 24.6 ± 2.3 s. Because the fill rates varied, the time is

shown in these Figures in a nondimensional form. The initial time is taken to be when the front passes a line in the square entry channel 0.16 cm from the entrance of the distributor. Here, one can see the effects of changing the distributor geometry. In Figure 23 the liquid has just filled the distributor. As in the numerical results, all of the modified geometries help flatten the leading front, especially Meshes 2 and 4. Mesh 2 also fills the distributor with the fastest relative time.

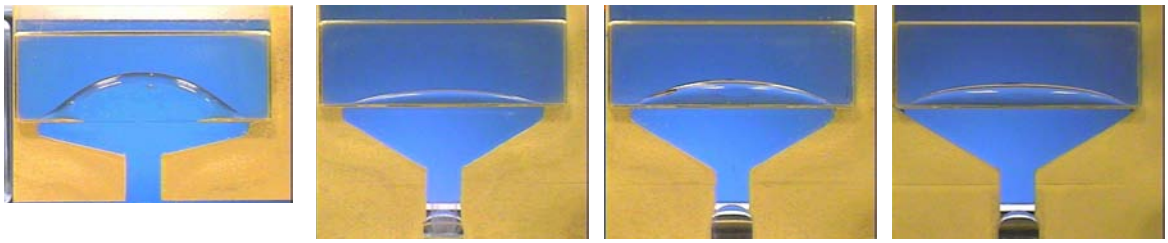

Figure 23. Comparison of the effect of distributor geometry on the shape of the fluid front entering the mold for vertical mold orientation.

Figure 24 shows the times at which the leading front hits the wall opposite the injection port. In this case the front in Mesh 2 takes the longest relative time to reach this stage. The other geometries once again follow the same pattern as before, with Mesh 4 closest to Mesh 2 and the original mesh the most different from Mesh 2. At this point, the fluid has wetted more of the side walls with the Mesh 2 and 4 geometries and the front is flatter.

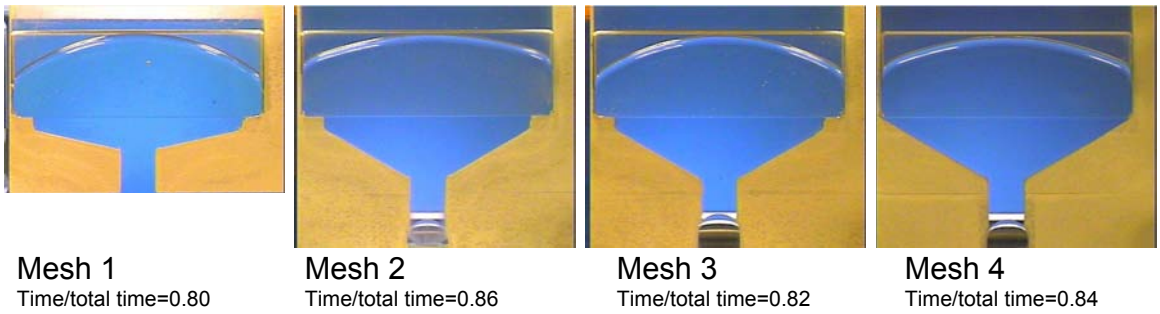

Figure 24. Comparison of the effect of distributor geometry on the time it takes to reach the wall farthest from the injection port for vertical mold orientation.

Figure 25 shows the locations of the voids remaining in the mold once filled but without any over pressure (a relative time of 1). Small bubbles away from the corners are artifacts of the syringe loading process. The voids in geometries with redesigned distributors still remain in the same locations as those seen in the original geometry. The relative areas of the bubbles on the images, which reflect the volume of air trapped, were determined and

compared quantitatively in Table 4. One pixel resolution represents about 1×10^{-5} cm^2. All redesigned distributors result in smaller bubbles in the upper corners than those in the original mesh. The lower bubbles of Mesh 2 are also smaller, whereas those in Mesh 3 are approximately the same as those in the original geometry.

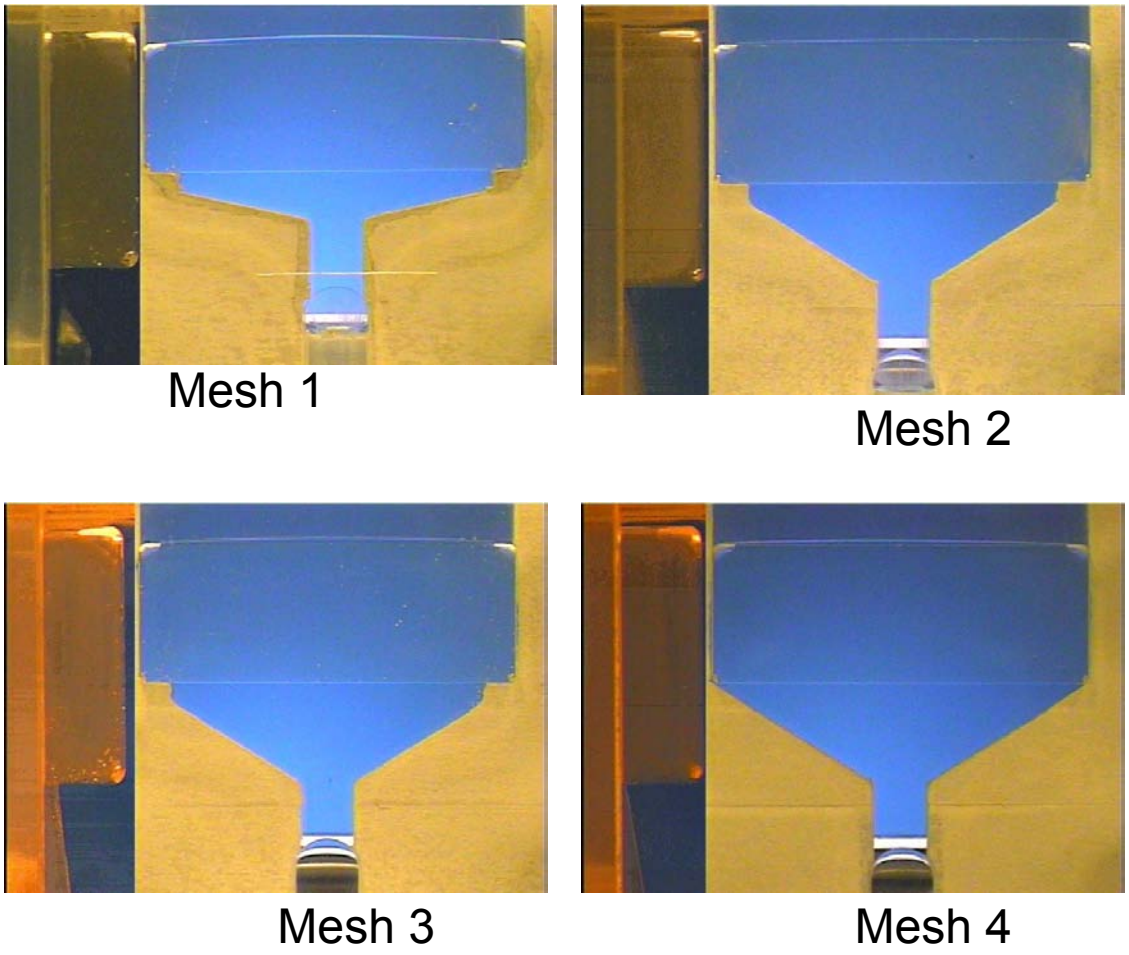

Figure 25. Voids remain in the front upper and lower corners of each geometry for the vertical mold orientation.

Table 4. Bubble sizes remaining in the corners for vertical mold orientation

Geometry	Area Upper Corners (cm^2)	Area Lower Corners (cm^2)
Original	0.0153 ± 0.0012	0.0020 ± 0.0005
Mesh 2	0.0086 ± 0.0007	0.0012 ± 0.0002
Mesh 3	0.0128 ± 0.0005	0.0021 ± 0.0001
Mesh 4	0.0128 ± 0.0001	0.0019 ± 0.0003

Next we experimented with the orientation of the mold. Molds were turned so that the distributor was perpendicular to gravity on the lower surface and the vent was moved to be on the upper surface. Results for the original mesh showed that orientation with respect to gravity had a large impact on the likelihood of voids remaining in the corners of the mold. Figure 26 shows representative video frames at three stages of the fill: 1) when the distributor was completely filled, 2) when the front hit the far wall, and 3) when the liquid began to exit through the vent and the sides had completely wetted. Because the fill rates varied, the time again is shown in a nondimensional form. The time it took to completely fill the original geometry in the horizontal position was 23.3 ± 0.9 s, to fill the geometry of Mesh 2 was 28.9 ± 1.5 s, and to fill the geometry of Mesh 3 was 27.3 ± 1.8 s.

The top views of the horizontal orientation show that the liquid wets the top later than the bottom. The oval area of the middle image in Figure 26A indicates where the liquid has wetted the upper surface. The side views are more difficult to interpret because of the lighting challenges accompanying trying to see through the thickest section of the mold. However, the dark areas of the side view are where the liquid has wetted the sides.

It is interesting to note that the horizontal alignment causes the front to hit the far wall before even wetting the sides at all. In other words the front was less "flat" entering the mold from the distributor. Nevertheless, the results also show that the horizontal orientation, with the vent on top and the distributor entrance on bottom, resulted in bubbles only in the upper corners nearest the distributor. When oriented vertically, bubbles are trapped in corners both opposite the distributor and opposite the vent. The bubbles nearest the distributor with the horizontal orientation are approximately the same size as the bubbles trapped in the upper corners opposite the vent in the vertical orientation.

The effect of distributor geometry on the filling in the horizontal orientation is shown in Figures 27 and 28, which correspond to Figures 23 and 24 in the vertical orientation. Here Mesh 4 was not available for comparison. Again the geometry of Mesh 2 results in the flattest front entering the mold from the distributor (Figure 27). The front reaches the back wall at approximately the same time using the distributors of Mesh 2 and 3. By the time the front reaches the back wall both modified geometries result in more liquid filling the mold than with the original geometry; however, Mesh 2 results in somewhat more than Mesh 3 (Figure 28).

A

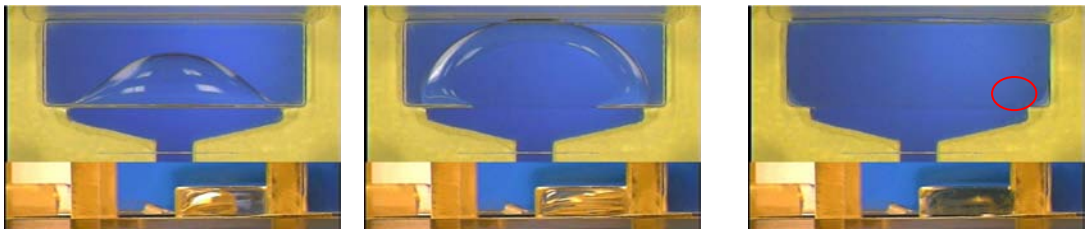

Time/total time=0.26 Time/total time=0.82 Time/total time=1.0

B

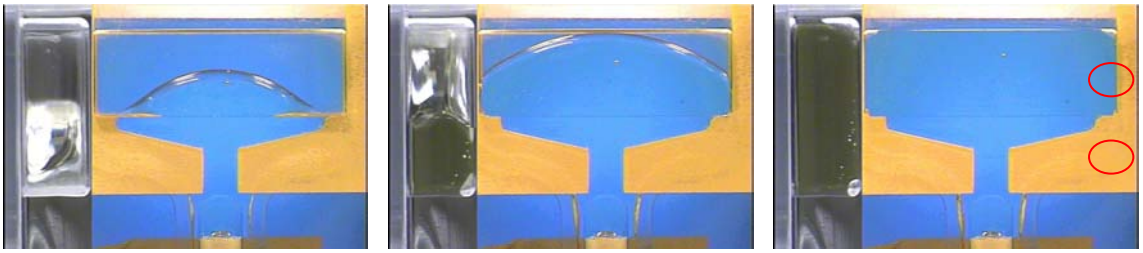

Time/total time=0.33 Time/total time=0.81 Time/total time=1.0

Figure 26. Original geometry (Mesh 1) oriented horizontally (A) and vertically (B). Images on the left show when the distributor fills completely, middle images show when the front first hits the back wall, and images on the right show when the part is filled to the point that the fluid leaves the vent area through the entire length of the vent. Bubbles left in the corners are circled in red.

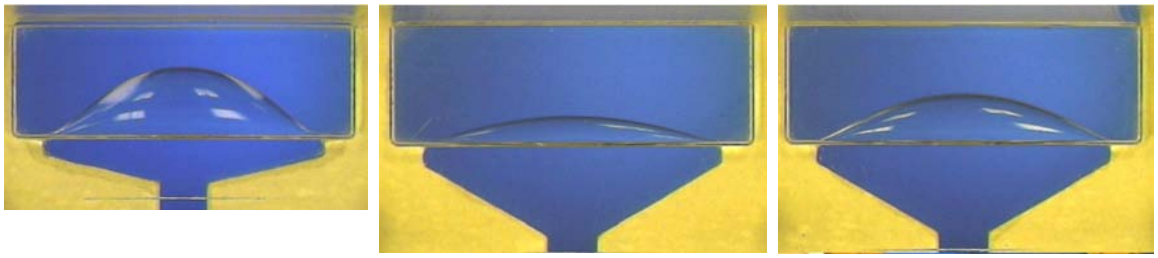

Mesh 1 Mesh 2 Mesh 3

Time/total time=0.26 Time/total time=0.13 Time/total time=0.22

Figure 27. Comparison of the effect of distributor geometry on the shape of the fluid front entering the mold in a horizontal orientation.

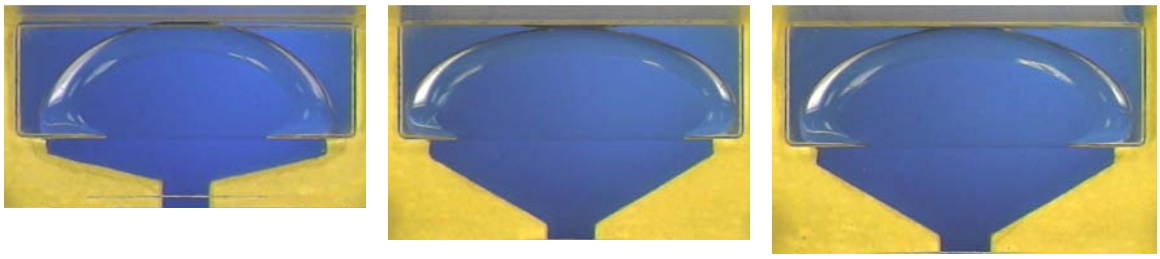

Figure 28. Comparison of the effect of distributor geometry on the time it takes to reach the wall farthest from the injection port in a horizontal orientation.

Sizes of the bubbles left in the various geometries in the horizontal orientation are listed in Table 5. Comparing these values with the measurements in Table 4, one can see that the amount of gas left in the vertical orientation is roughly the same as that in the horizontal orientation, although in the horizontal orientation there are fewer bubbles. Bubbles observed in other locations than the corners are almost always artifacts of the syringe loading process. Only once, a bubble was trapped somewhere in the center of the mold because of uneven wetting, and this phenomena was not observed again (Figure 29).

Table 5. Bubble sizes remaining in horizontal orientation

Geometry	Area (cm^2)
Original	0.0189 ± 0.0002
Mesh 2	0.0111 ± 0.0002
Mesh 3	0.0123 ± 0.0017

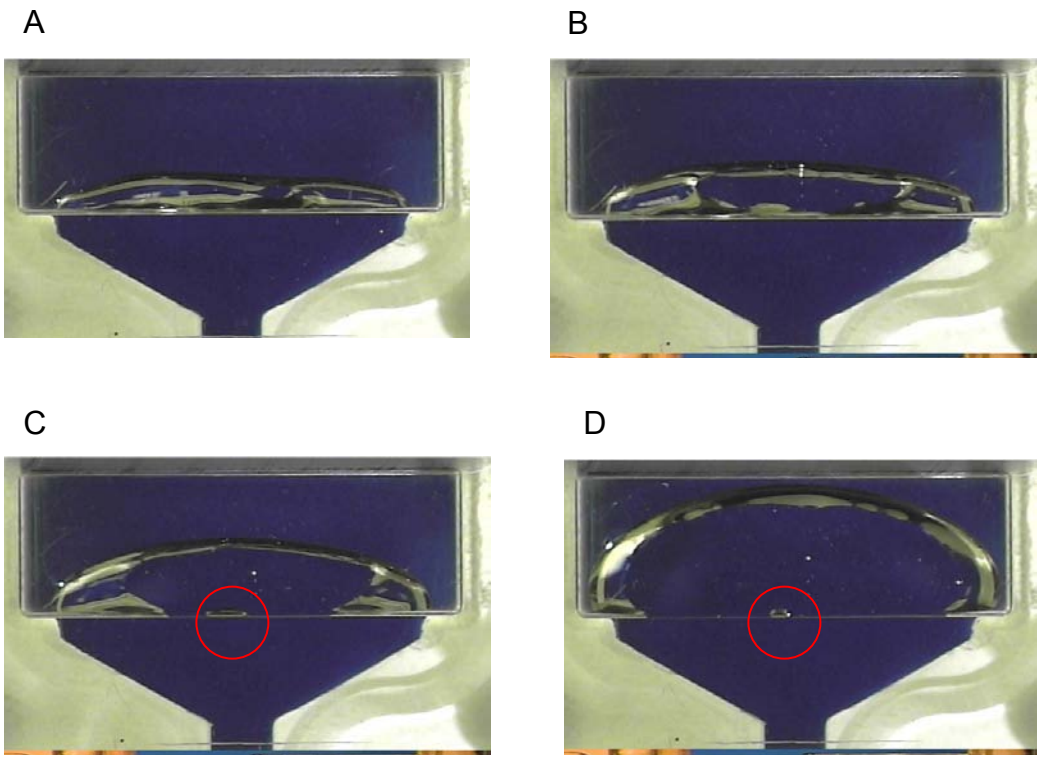

Figure 29. Uneven wetting of top surface in the horizontal orientation left a bubble (circled in red) in this time sequence from A-D. This was the only instance that this was observed.

5. Validation Simulations

For the validation simulations we use a Blake wetting condition (Blake and Haynes, 1969) for the wall velocity in the region of the contact line.

$$v_{wall} = v_o \sinh(\bar{\gamma}(\cos\theta_s - \cos\theta)) - \tau \frac{\partial v_{wall}}{\partial t} \tag{20}$$

The Blake model fit to the dynamic wetting data for UCON oil on acrylic given in Figure 22 is a wetting speed of 0.0013cm/s and scale factor γ of 2.29 with a static contact angle of 42.4^o. The value of the tangential wall velocity ramps from zero at a level set length scale away from the contact line to v_{wall} from Equation (20) at the contact line. Away from the contact line we revert to no slip for the tangential wall velocity boundary condition. The normal velocity is enforced as no penetration everywhere. The shape of this ramp must be smooth in order to get a realistic wetting line that shows a smooth transition from the contact line to the bulk flow. For a sharp transition from slip to Blake, we ended up with unphysical looking cusps in the interface shape near the wall. The transient terms allows smooth movement of the contact line. The τ parameter is taken to be on the order of the time step.

Properties used for the validation simulations were the measured values discussed in the experimental section. The density and viscosity of the displaced gas phase were taken as fictitious value of 1000 smaller than the liquid phase density and viscosity. These values are summarized in Table 6.

Table 6. Material properties used for validation simulations

Material Property	**Value**
Density of liquid	1.09 g/cm^3
Viscosity of liquid	390 Poise
Density of gas	0.0011 g/cm^3
Viscosity of gas	0.39 Poise
Wetting speed, v_o	0.0013 cm/s
Blake scale factor, γ	2.29
Static contact angle	37.3^o
Surface tension	42.4 dyne/cm
Inflow pressure	1e6 dyne/cm^2

At 100^{o}C, the viscosity of air is 2.17x10^{-4} Poise and the density of air is 0.0012 g/cm^{3}, thus our second phase properties are very close for density, but three orders of magnitude too high for viscosity. The numerical method fails to converge for values of the liquid/gas viscosity ratio of less than 1000 for a diffuse interface implementation of the level set equations.

For the inflow condition, we used a constant inflow pressure of 1.0 e6 dyne/cm^{2}. This value was chosen to roughly match the horizontal fill time of 23 seconds in the original mesh and then used for all other meshes and geometries. A shooting method was used, where different values of the inflow pressure were used and the solution was examined to see if it filled in the correct time. This required many simulations to be run. It is believed that the actual boundary condition for the experiments is somewhere between a constant velocity and constant pressure condition, but this is hard to replicate numerically. From the simulations we did find that the velocity changed quickly in the beginning for the pressure inflow boundary condition and subsequently reached a steady value.

The simulations were run using ARIA with PSPP pressure stabilization and the BiCGSTAB/ILU solver-preconditioner pair. This stabilization method has shown good scalability and robustness, allowing for a fast Krylov based solver with low levels of preconditioning, all of which means quick turn around times for solutions. The validation runs were made on 64 processors of Thunderbird and ran in less than 3.5 hours. This was a significant breakthrough from the month long calculations necessary for PSPG stabilization and allowed us to do real time design and sensitivity calculations for parameters such as wetting speed, second phase viscosity, level set length scale and inflow pressure.

The time to fill the mold for the vertical orientation for Mesh 1, Mesh 2, and Mesh 3 are 15.2s, 17.5s, and 13.2s, which was much faster than the experimental values of 24.6s, 26.9s, and 24.6s. We defined our fill time as when the vent had filled completely to a distant of the level set length scale or two elements. Unfortunately, the numerical fill times are difficult to obtain accurately as the gas phase viscosity makes a large difference in how fast a simulation will fill for the same value of pressure. For instance, when we reduced the second phase viscosity by a factor of 10 we got an increase in the inflow velocity when keeping all other parameters constant. So the fact that the gas phase is harder to push out than it is for the experiments, adds a great deal of uncertainty to the fill times. However, we hope to be able to predict trends. Figure 30 shows the effect of the distributor geometry on the meniscus shape for Mesh 1, Mesh 2, and Mesh 3 in a vertical orientation.

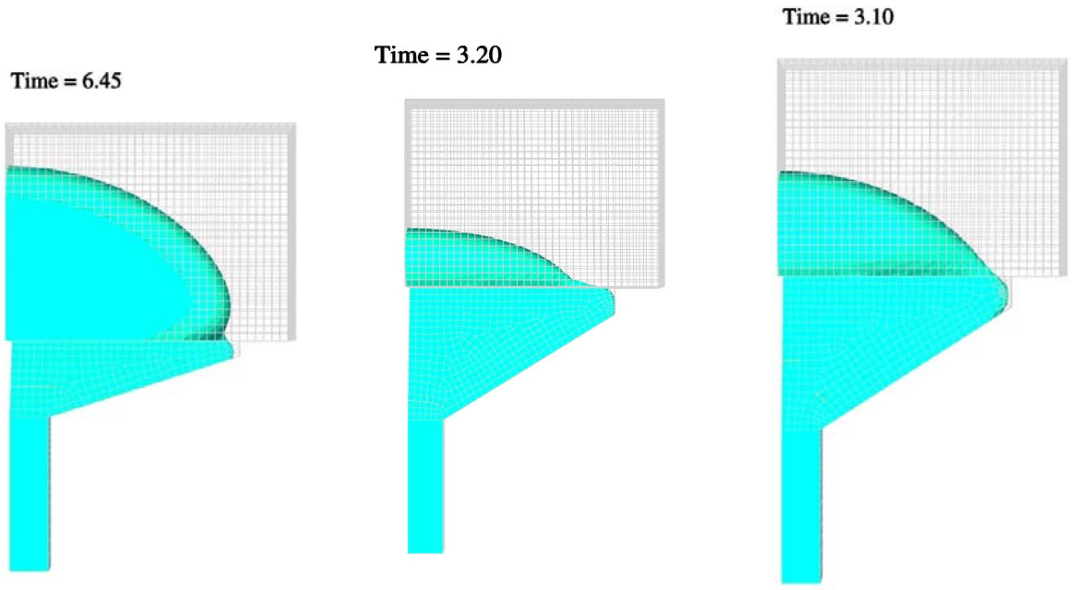

Figure 30. Free surface profile after filling the distributor for Mesh 1, Mesh 2, and Mesh 3 for vertical mold orientation.

Comparing Figures 30 and 23, the numerical and experimental version of this profile, we can see that the simulations are catching the correct trends of the physical situation. The original mesh takes the longest fractional time to fill the distributor, 42%, and gives the most bulging front shape. Mesh 2 is an improvement, taking 18% of the time to fill the distributor, while Mesh 3 is somewhere in between at 24%. The values for the experimental distributor dimensionless fill times are 32%, 13%, and 24%, so the simulations are also capturing the correct trends for fill time though they are not quantitative. The shape of the meniscus for Mesh 1 has more of a bulge at the edge of the distributor than the experimental one, which looks as if the front is pinned at the distributor.

We can also look at the profiles and dimensionless time to hit the back wall. These results are given in Figure 31.

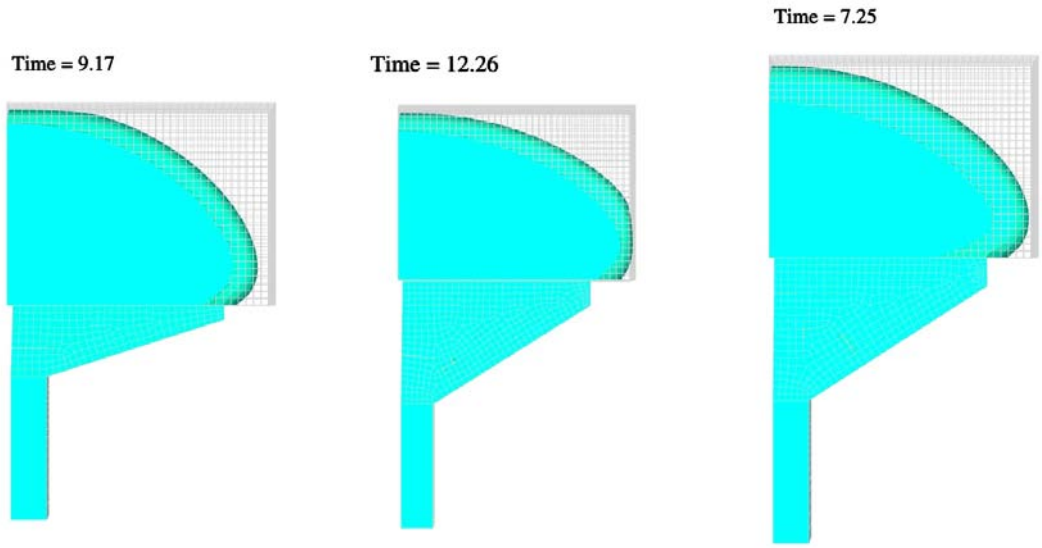

Figure 31. Free surface profile after hitting the back wall for Mesh 1, Mesh 2, and Mesh 3 for vertical mold orientation

Comparing Figure 31 to Figure 24, for the simulation versus experiment, we can see difference in the meniscus shape. The numerical interface reaches the back wall for Mesh 1 and Mesh 3, before it wets the side wall and Mesh 2 has a flatter profile in the experiments than the simulations. The percentage time to reach the back wall for the simulations on Mesh 1, Mesh 2, and Mesh 3 are 60%, 70%, and 55% compared to 80%, 86% and 82% for the experiments. Again, we are capturing the correct trends, but are still unable to match quantitatively.

Figure 32 shows the full meniscus shape and void locations for the simulations on Mesh 1, Mesh 2, and Mesh 3.

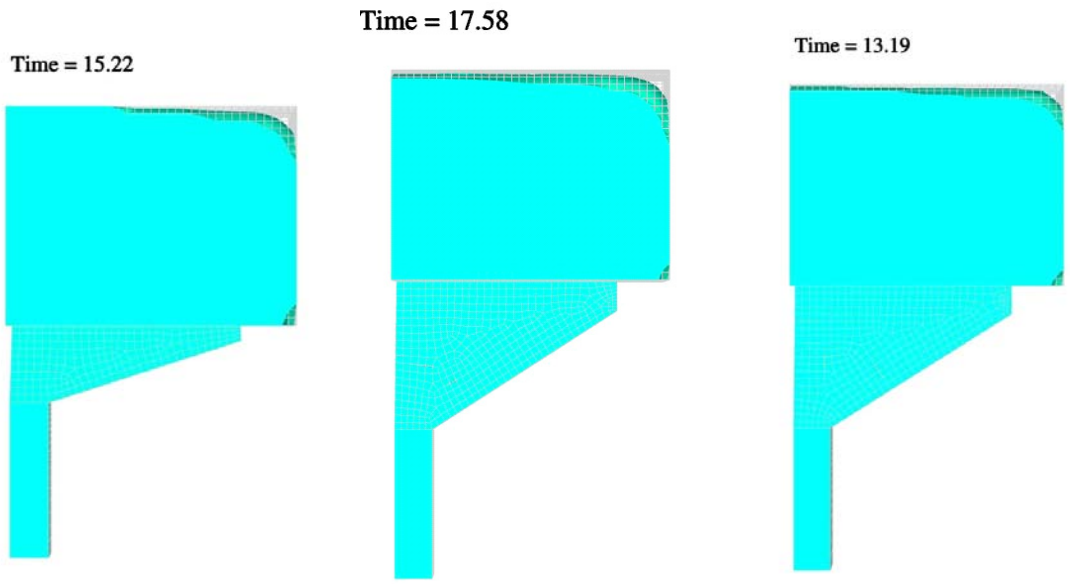

Figure 32. Final void location and front profile for Mesh 1, Mesh 2, and Mesh 3.

The void in the corner near the distributor does eventually fill in, since its size is less than the level set length scale and we are using a diffuse interface method. The larger void at the vent area never fills in as the viscous gas phase gets trapped away from the vent by the paste. For the numerical solutions it is hard to make any predictions about void size, though we can say that for similar values of the dimensionless time the voids for Mesh 2 will be smaller than Mesh 1, with Mesh 3 being somewhere in between, which does follow the experimental trend.

We also examined the horizontal orientation numerical, which gave fill times for Mesh 1, Mesh 2, and Mesh 3 of 21.4s, 23.1s, and 22.2s compared to 23.3s, 28.9s, and 27.3s for the experiments. Again, we follow the trends of the experiment, but do not match quantitatively. Mesh 2 seems to take a longer time to fill for the experiment than one would predict numerically. Figure 33 shows a comparison of the profiles for Mesh 1 in a vertical and horizontal orientation.

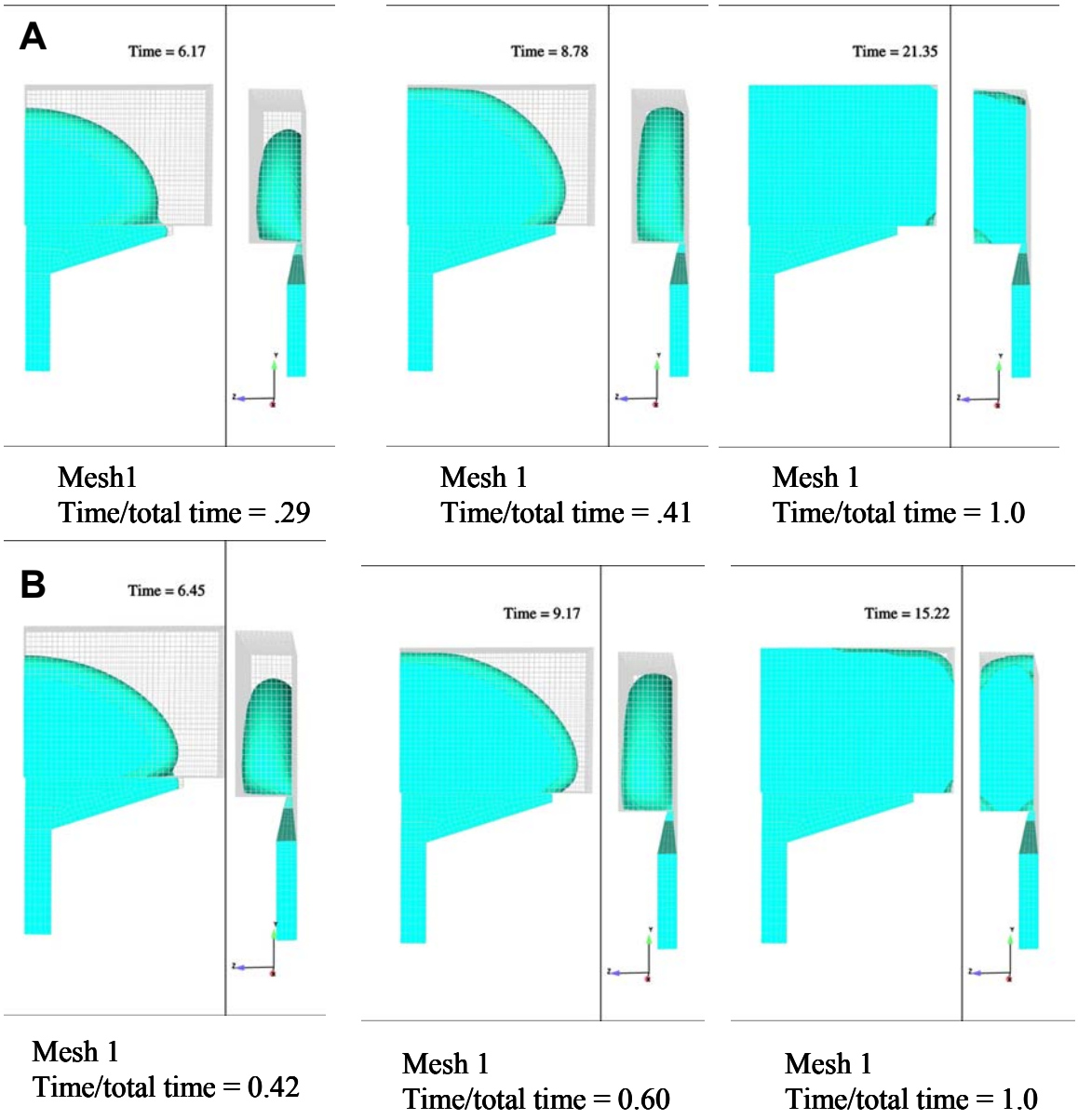

Figure 33. Mesh 1 oriented horizontally (A) and vertically (B). Leftmost pictures show profiles when the distributor is filled, middle shows profile when the fluid hits the back wall, and rightmost pictures show final profile. Both front and side views are given to highlight void location.

Comparing Figure 33 to the experimental equivalent, Figure 26, we can see that we have quantitative differences but do match some trends. The numerical meniscus shape leaving the distributor looks similar to the experimental profile as it bulges more in the center for the horizontal orientation, though the simulation is less dramatic. The numerical profiles when the fluid first hits the back wall are flatter for the vertical orientation than the horizontal, though the vertical should be even flatter to match the data. The numerical solutions predict two voids for each orientation, though the experiments do not show a

second void for the horizontal orientation near the vent, though this void may just be difficult to see experimentally. Or conversely, the horizontal void at the outflow may be an artifact of the numerical method as we have a difficult balance at the outflow between wetting forces, gravity, the gas phase viscosity, and the material flowing out the vent. Also, our numerical vent is not the same size as the experimental one.

Figure 34 shows the meniscus profiles for Mesh1, Mesh 2, and Mesh 3 after filling the distributor for the horizontal orientation.

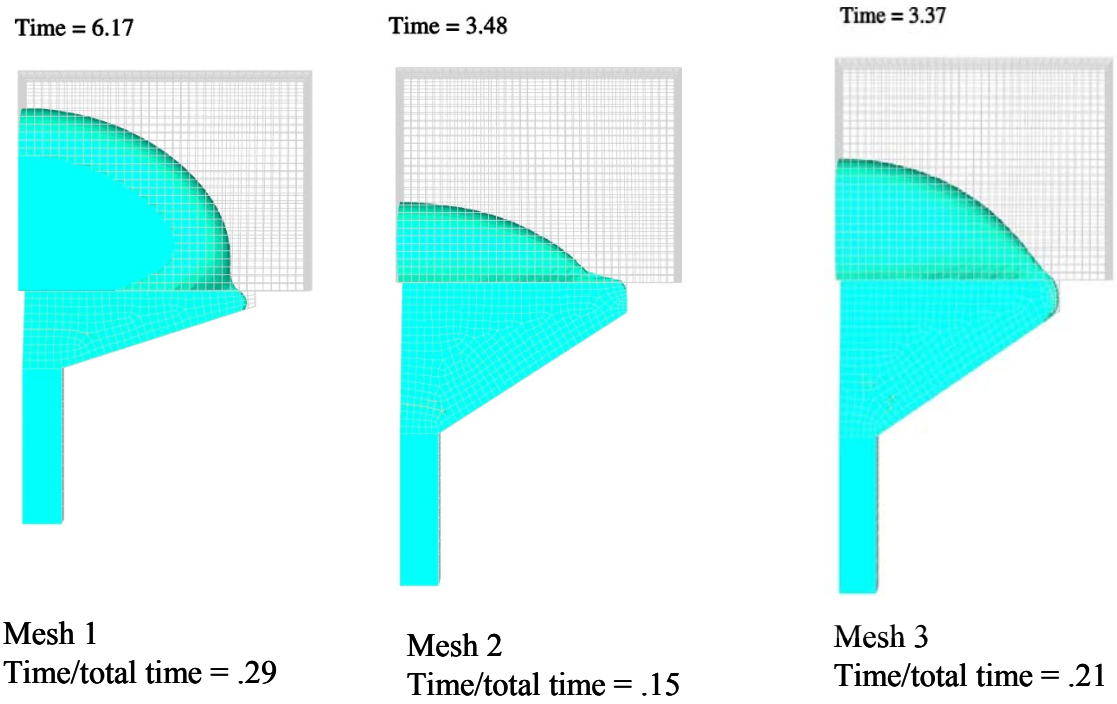

Figure 34. Free surface profile after filling the distributor for Mesh 1, Mesh 2, and Mesh 3 for horizontal mold orientation.

Comparing Figures 34 and 27, the numerical and experimental version of this profile, we can see that the simulations are catching the some of the correct trends of the physical situation. Mesh 1 shows the most pooling at the center of the mold, Mesh 2 has a flatter profile as does Mesh 3. The experiments predict Mesh 3 to be in between Mesh 1 and Mesh 2, and the simulations also follow this trend. The dimensionless times to fill the distributor numerically for Mesh 1, Mesh 2, and Mesh 3 are 29%, 15%, and 21% compared to 26%, 13% and 22% for the experiments. In general, the simulations predict the vertical filling to be faster overall than the horizontal by several seconds for each of the geometries, whereas the experiments are faster in the vertical for Mesh 2 and 3, but slower for Mesh 1. This could have resulted from some experimental errors.

Figure 35 shows the free surface profile as the fluid hits the back wall for Mesh 1, Mesh 2, and Mesh 3 in the horizontal orientation. The dimensionless times it takes to hit the back wall for Mesh 1, Mesh 2, and Mesh 3 are 41%, 55%, and 52% compared to values of 82%, 71%, and 70% for the experiments seen in Figure 28.

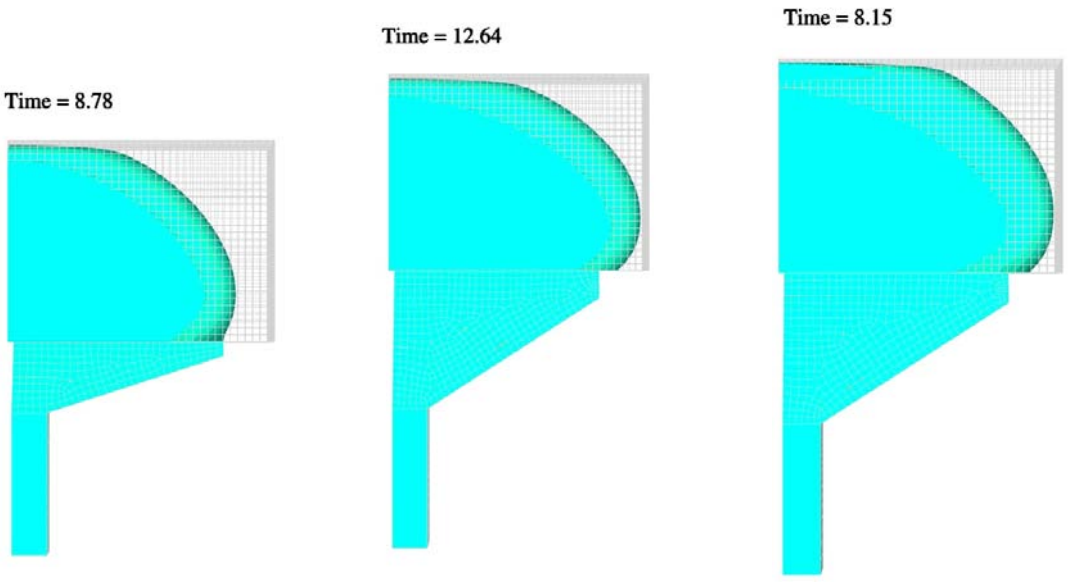

Figure 35. Free surface profile after hitting the back wall for Mesh 1, Mesh 2, and Mesh 3 for horizontal mold orientation.

For the simulations, Mesh 1 hits the back wall for the smallest dimensionless time while Mesh 2 and Mesh 3 take about the same time. For the experiments, Mesh 1 takes the longest time, while Mesh 2 and Mesh 3 do take about the same time. So for this case, we are capturing one trend, but not the differences between Mesh 1 and Mesh 2.

Table 7 summarized the fill times to reach the distributor, back wall, and complete fullness for the simulations and experiments for vertical and horizontal orientations on all three meshes.

Table 7. Summary of fill times for experiment and simulations to reach the distributor, the wall and completely full

Mesh	Orientation	Expt. Fill Time - Full	Expt. % Time - Dist	Expt. % Time - Wall	Sim. Fill Time- Full	Sim. % Time - Dist	Sim. % Time - Wall
Mesh 1	Vertical	24.6s	32%	80%	15.2s	42%	60%
Mesh 2	Vertical	26.9s	13%	86%	17.5s	18%	70%
Mesh 3	Vertical	24.6s	24%	82%	13.2s	24%	55%
Mesh 1	Horizontal	23.3s	26%	82%	21.4s	29%	41%
Mesh 2	Horizontal	28.9s	13%	71%	23.1s	15%	55%
Mesh 3	Horizontal	27.3s	22%	71%	15.6s	21%	52%

From Table 7 we can see that we capture some of the correct trends, especially for the vertical orientation, though some features elude us like the time to fill to the back wall for Mesh 1 in the horizontal orientation. Future work we will include both more careful experiments as well as use of advanced features in ARIA to allow for smaller values of the gas phase viscosity, such as sharp integration and XFEM that were available in GOMA for 2D, when such features are available in 3D. These advanced features have allowed us to run problems where the gas phase could even be ignored, such as in a vacuum.

Our validation exercise gave us enough confidence in our simulations to undertake numerical solutions for the actual material properties and orientation. The predictions were more accurate for the vertical orientation, and the actual process has the mold in the vertical orientation. Simulations for the paste are discussed in the next section.

6. Results for PZT paste

We did numerical simulations using the actual property values for the PZT paste, but with a Newtonian viscosity chosen from the nonisothermal, non-Newtonian simulations discussed in section 3.2. The properties used are summarized in Table 8.

Table 8. Material properties used for PZT paste simulations

Material Property	**Value**
Density of liquid	4.5 g/cm3
Viscosity of liquid	4000 Poise
Density of gas	0.0045 g/cm3
Viscosity of gas	4.0 Poise
Wetting speed, v_o	1.0 cm/s
Blake scale factor, γ	2.29
Static contact angle	40^o
Surface tension	42.4 dyne/cm

Again the values of the gas properties are fictitious and used to maintain numerical stability. The numerical method fails for viscosity ratios between the liquid and gas of greater than 1000. The real ratio between the liquid phase and the air is on the order of 1.e7. The wetting properties for the PZT paste have not been measured, so we use values similar to the UCON oil for these properties except with a faster wetting speed of 1.0cm/s, since the PZT fill the mold in less than 0.5s. For the PZT paste simulations we use a constant velocity boundary condition of 190cm/s at the inflow.

The results for the real material are given in Figure 36 for Mesh 1 in the vertical orientation.

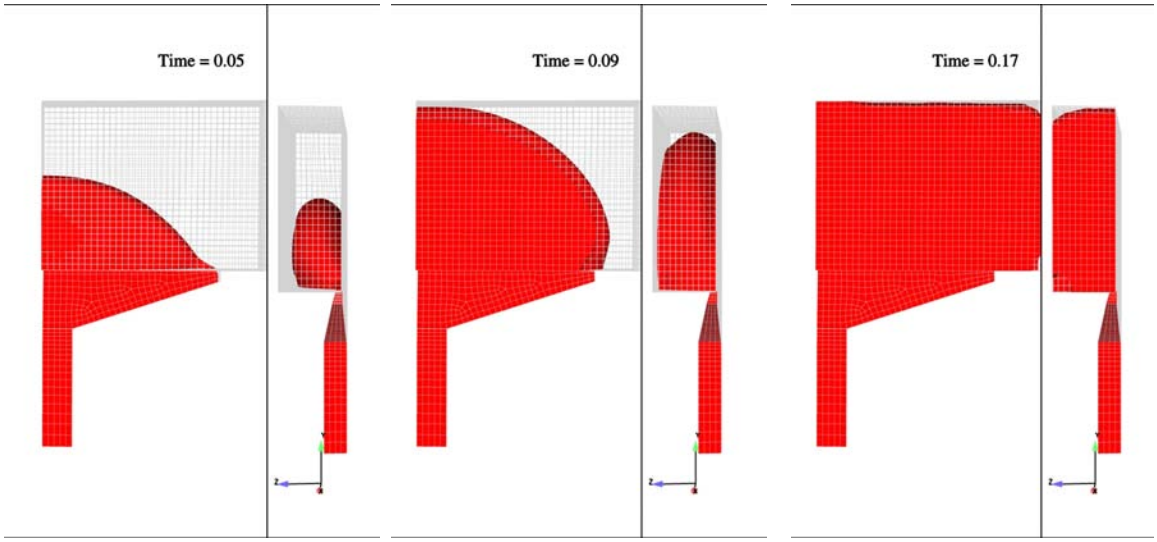

Mesh 1
Time/total time = .29

Mesh 1
Time/total time = .53

Mesh 1
Time/total time = 1.0

Figure 36. Meniscus shape as a function of time for real PZT properties on Mesh 1 in vertical orientation.

From Figure 36, we can see that once the fluid fills the distributor it has just barely started to wet the front wall. The material then hits the back wall without touching the side walls, perhaps due to the high viscosity of the gas phase making wetting the side walls difficult. The final free surface profile again shows voids located at the outer corners of the mold near the distributor and near the vent.

We ran the PZT paste simulation on the refined version of Mesh 1 shown in Figure 37.

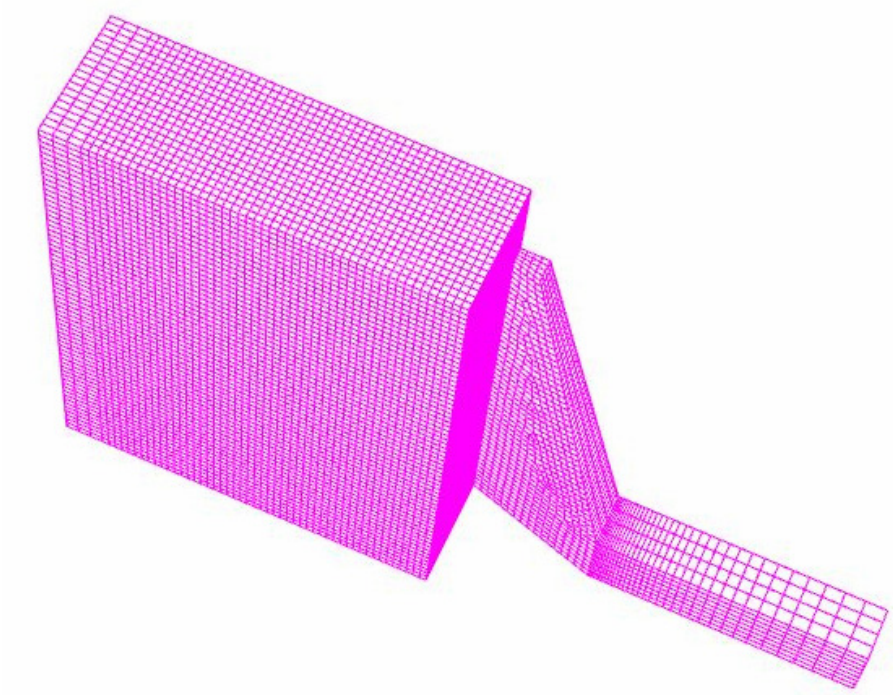

Figure 37. Refined version of Mesh 1

The results on the refined mesh are given in Figure 38 for the profiles to fill the distributor and hit the back wall. The simulation failed a Newton step before the mold was completely filled, a problem which cannot currently be recovered from in ARIA, so the final profile is given instead.

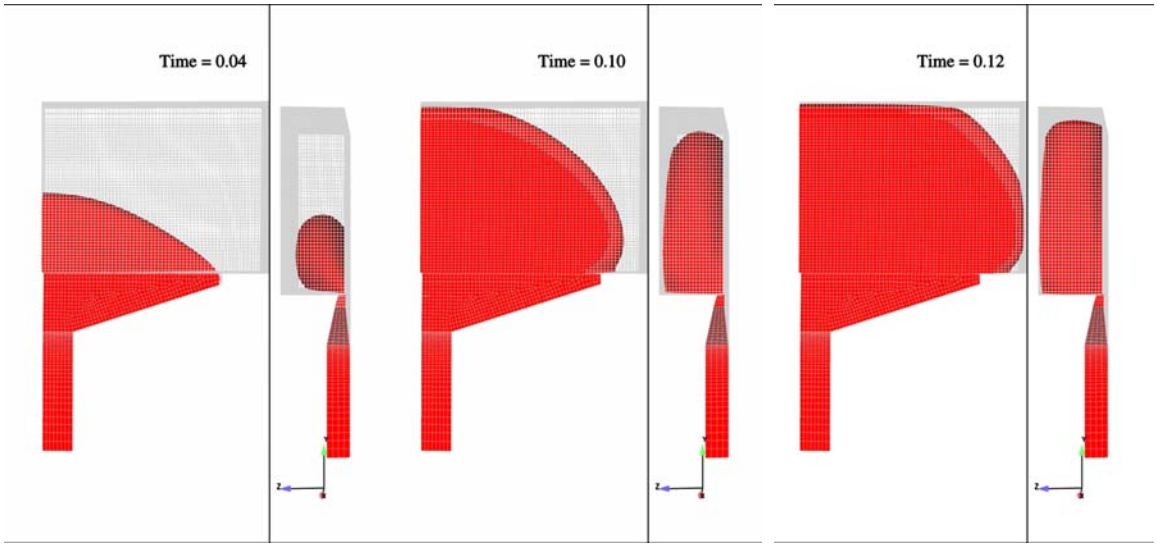

Mesh 1 - refined
Time/total time = .24

Mesh 1- refined
Time/total time = .59

Mesh 1 - refined
Time/total time = .71

Figure 38. Meniscus shape as a function of time for real PZT properties on a refined version of Mesh 1 in vertical orientation. Simulation failed to converge before the mold was filled. The last time value was 0.12s. We assume that the mold would have filled in 0.17s as the unrefined version did.

The refined mesh profiles look very similar to the unrefined mesh ones and occur at similar dimensionless times, giving us hope that our unrefined mesh results are convergent and meaningful. It is unfortunate that the simulation failed on the refined mesh, as it would be interesting to examine the solution as it hits the side wall and reached the outflow and to compare the void location and size to the unrefined mesh.

7. Conclusions and Future Work

In this report, we have investigated the injection molding of a PZT ceramic paste using experiments and simulations. Capillary rheometry has been used to characterize the paste, whose behavior ranged from solid below 94^{o}C, to soft matter from 94-150^{o}C, and fluid about 160^{o}C. These data were then fit to a Carreau model that takes into account both shear-thinning and temperature changes. No constitutive model can hope to fit the range of behavior, but the Carreau model will capture the correct trends with temperature and shear rate. The isothermal version of the Carreau fluid was used in 2D finite element-level set simulations to examine the shape of the free surface with time. These results were compared to Newtonian simulations for a viscosity similar to the wall viscosity of the Carreau fluid and it was determined that both fluids gave similar free surface shapes, thus for 3D we could simplify things and run Newtonian simulations and still predict the correct free surface shape. Nonisothermal 2D Carreau fluid simulations were carried out to determine what viscosity should be used for the 3D Newtonian simulations. This value depended heavily on what type of wall boundary conditions were used, either room temperature walls or applying a heat flux based on a heat transfer coefficient. The results form these two boundary conditions varied greatly from predicting that the fluid cooled off at early times to the room temperature or the fluid stayed as hot as the inflow temperature. A thermal analysis was carried out that implied the wall temperature would be hotter than room temperature, more like 320K. For the thermal and level set simulations, it was decided that the wall viscosity would be roughly 4000 Poise.

In the 3D world, initial transient simulations suggested that the fluid pooled in the center of the mold and would potentially leave voids. These simulations were enlightening, but took several months to run on 4 processors of a HP workstation using a preconditioner /solver combination of ILUT/GMRES with fill factors of 3 and PSPG stabilization. We explored possible redesign of the distributor using faster 3D steady-state simulations. The pressure and velocity profiles from these simulations led us to believe that a longer distributor length would allow for a flatter, more monotonic meniscus shape on entering the cavity. We also investigated a longer distributor that also had a larger entrance into the cavity of the mold; this redesign was also an improvement over the initial mesh. 3D transient simulations did verify the conclusion from the steady-state simulations.

Validation experiments were carried out on the three different distributor designs using a UCON lubricant, which is a Newtonian fluid. It was found that the new designs were an improvement over the initial design in that they showed flatter meniscus shapes as they entered the mold and left smaller voids in the vertical orientation. Experiments also investigated Mesh 1, Mesh 2, and Mesh 3 in a horizontal geometry. It was found that the horizontal orientation seemed to eliminate the void near the vent, though the amount of trapped gas was roughly the same in both the vertical and horizontal orientations.

Validation simulations were carried out to closely follow the experiments. The simulations did capture many of the experimental trends, though quantitative agreement was lacking. We feel that the lack of agreement between the experiment and simulation probably stems from several factors, including the diffuse interface, the high value for the gas phase viscosity, and the wetting parameters. For future work, we plan to investigate using an

XFEM level set method that allows for sharp integration of the interface and discontinuous values of pressure and velocity at the interface, which will then accommodate higher ratios of the fluid to gas viscosity. We also plan to undertake a wetting study in a simplified geometry to allow us to test our wetting model without requiring massively parallel computations.

Each simulation took 4 hours to run on 64 processors of Thunderbird using ILU/BiCGStab and PSPP stabilization. This speed up allowed us to run sensitivity studies for parameters such as geometry, orientation, wetting speed, and inflow pressure, which would have been previously impossible with our 3 month turn around times. Other improvements in the numerical method have allowed us to look at fluid to gas viscosity ratios of 1000 to 1, when previously the best we could do was 10 to 1, though even higher ratios will be necessary for predictive simulations.

The simulations using the paste properties, with the Newtonian material model, led us to believe that two voids would be trapped for the original mesh in a vertical orientation. A refined mesh confirmed the results from the original mesh, though the simulation failed when the paste came near the side wall. From the simulations and experiments, we believe a redesign of the mesh with a longer distributor would be an improvement over the current design.

8. References

Baer, T.A., D.R. Noble, R.R. Rao, and A.M. Grillet, "A Level Set Approach to 3D Mold Filling of Newtonian Fluids," Proceedings of the ASME Symposium on Flows in Manufacturing Processes, Honolulu, Hawaii, July 6-10, 2003.

Bird, R.B., R. C. Armstrong, and O. Hassager, *Dynamics of Polymeric Liquids*, Wiley, New York, New York (1987).

Blake, T.D. and J.M. Haynes, "Kinetics of liquid/liquid displacement ," J. Colloid Interface Sci., 30, 421 (1969).

Brooks, C.F., personal communications, Sandia National Laboratories, Albuquerque, NM (2006).

Halbleib, L. L., "The Effects of Processes Parameters on Injection-Molded PZT Ceramics Part Fabrication-Compounding Process Rheology, SAND2005-2864, May 2005.

Ferguson, J. and Z. Kemblowski, *Applied Fluid Rheology*, Elsevier Applied Science, New York, pp. 52-55, (1991)

Rao, R. R., L. A. Mondy, P. R. Schunk, P. A. Sackinger, D. B. Adolf, "Verification and Validation of Encapsulation Flow Models in GOMA, Version 1.1," Sandia National Laboratories, SAND2001-2947, October 2001.

William, M.L., R.F. Landel, and J.D. Ferry, "The Temperature Dependence of Relaxation Mechanisms in Amorphous Polymers and Other Glass-Forming liquids," *J. Am. Chem. Soc.*, 77, 3701, 1955.

Sethian, J.A., *Level Set Methods and Fast Marching Methods*, Cambridge University Press, (1999).

Jacqmin, D., "Three-dimensional computations of droplet collisions, coalescence, and droplet/wall interaction using a continuum surface-tension method," AIAA-95-0833.

Notz, P.K, S.R. Subia, M.M. Hopkins, D.R. Noble, H.K. Moffat, D. Neckles, http://aria.sandia.gov/.

C.R. Dohrmann and P.B. Bochev, "A stabilized finite elements method for the Stokes problem based on polynomial pressure projections," International Journal for Numerical Methods in Fluids, 46, 183 (2004)

Sartor, L., Slot Coating: Fluid Mechanics and Die Design, University of Minnesota, Ph.D. Thesis, (1990).

Schunk, P.R., P.A. Sackinger, R.R. Rao, K.S. Chen, T.A. Baer, D.A. Labreche, A.C. Sun, M.M. Hopkins, S.R. Subia, H.K. Moffat, R.B. Secor, R.A. Roach, E.D. Wilkes, D.R. Noble, P.L. Hopkins, and P.K. Notz, "GOMA 4.0 – A Full-Newton Finite Element Program for Free and Moving Boundary Problems with Coupled Fluid/Solid Momentum, Energy, Mass, and Chemical Species Transport: User's Guide," Sandia National Laboratories, SAND2002-3204, October, 2002.

Distribution:

1	MS0384	Art Ratzel	1500
1	MS0825	Wahid Hermina	1510
1	MS0834	Robert Tachau	1512
1	MS0834	Jaime N. Castañeda	1512
1	MS0834	Ray Cote	1512
1	MS0834	Carlton Brooks	1512
1	MS0834	Anne Grillet	1513
1	MS0826	Dan Rader	1513
1	MS0836	Ken Chen	1514
1	MS0836	Rick Givler	1514
1	MS0836	Matt Hopkins	1514
1	MS0836	Joel Lash	1514
5	MS0836	Lisa Mondy	1514
1	MS0836	David Noble	1514
1	MS0836	Pat Notz	1514
5	MS0836	Rekha Rao	1514
1	MS0836	Randy Schunk	1514
1	MS0380	Hal Morgan	1540
1	MS0382	Steve Gianoulakis	1541
1	MS0888	Joe Lenhart	1821
1	MS1245	Phil Cole	2453
1	MS1245	John Emerson	2453
1	MS0959	George Burns	2454
1	MS1245	Chris Diantonio	2454
1	MS1245	Pin Yang	2454
1	MS0829	Laura Halbleib	12337
1	MS9018	Central Technical Files	8944
2	MS0899	Technical Library	4536